Born-Oppenheimer molecular-dynamics simulations of finite systems: Structure and dynamics of $(H_2O)_2$

Robert N. Barnett and Uzi Landman
School of Physics, Georgia Institute of Technology, Atlanta, Georgia 30332
(Received 28 January 1993)

A method for calculations of the ground-state energy and structure of finite systems and for molecular-dynamics simulations of the evolution of the nuclei on the Born-Oppenheimer ground-state electronic potential-energy surface is described. The method is based on local-spin-density functional theory, using nonlocal pseudopotentials and a plane-wave basis set. Evaluations of Hamiltonian matrix elements and the operations on the wave functions are performed using a dual-space representation. The method, which does not involve a supercell, affords accurate efficient simulations of neutral or charged finite systems which possess, or may develop, multipole moments. Since the ground-state electronic energy and the forces on the ions are calculated for each nuclear configuration during a dynammical simulation, a relatively large time step can be used to integrate the classical equations of motion of the nuclei (1–10 fs, depending on the characteristic frequencies of the ionic degrees of freedom). The method is demonstrated via a study of the energetics, structure, and dynamics of the water dimer, $(H_2O)_2$, yielding results in agreement with experimental data and other theoretical calculations. In addition to the properties of the ground state of the dimer, higher-energy transition structures involved in transformations between equivalent structures of the $(H_2O)_2$ molecule, were studied, and finite temperature simulations of the dynamics of such transformations are presented.

I. INTRODUCTION

Molecular-dynamics (MD) simulations, where the phase-space trajectories for a system of interacting species (atoms, molecules, ions) are generated via numerical integration of the equations of motion,[1] open avenues for study of a broad scope of problems in a variety of areas,[2–5] such as materials science, condensed matter and chemical physics, statistical mechanics, hydrodynamics, and biophysics. Furthermore, MD simulations have proven useful for investigations of systems under equilibrium or nonequilibrium conditions, in different thermodynamic states (solids, liquids, and gases), in bulk environments as well as surfaces and interphase interfaces (solid/liquid, solid/vapor, liquid/vapor, and solid/solid such as grain boundaries), and for studies of systems characterized by different degree of aggregation (e.g., extended systems treated with the use of periodic boundary conditions, and finite atomic and molecular clusters).

In conventional MD simulations the classical equations of motion are derived from a Lagrangian or Hamiltonian description consisting of kinetic and potential energy terms (with auxillary terms in the case of constrained MD formulations[1]). In most early and many current uses, the interaction potentials between the particles are functions of the interparticle coordinates and may include pairwise, three-body, and higher-order terms, whose functional forms are related to the nature of interactions and bonding in the material under investigation.[2] These potentials are commonly determined by choosing a parameterized functional form on the basis of physical and chemical considerations and fitting the parameters to a given set of experimental and/or theoretically calculated data. Obviously, while most useful for many investigations, the applicability and predictive power of this approach is limited in circumstances where the system evolves into regions of configuration space not covered by the fitted data (e.g., potentials fitted to bulk properties may not be adequate to describe undercoordinated systems such as surfaces or clusters), although progress in constructing "environment-dependent" potentials has been realized.[6] Moreover, serious difficulties are encountered in investigations where electronic rearrangements occur, such as in chemical reactions or changes in the nature of bonding (e.g., a transition from covalent to metallic behavior as occurring in silicon upon transformation from the solid to the liquid state).

These considerations clearly point to the need to develop alternative simulation methods where the interatomic interactions underlying the dynamical evolution of the nuclear degrees of freedom are generated concurrently, consistently, and accurately as the simulation evolves. Therefore, in such methods determination of the potentials is an integral part of the simulation, rather than a separate preliminary step as in conventional MD simulations.

First-principle calculations of the total energy of a material and evaluation of the interatomic interactions between the atomic, or ionic, constituents require a quantum-mechanical description. Indeed, the development of methods for electronic-structure calculations of atomic, molecular, and condensed-phase systems has preoccupied scientists since the dawn of quantum mechanics, and to date there exists a vast arsenal of computational methodologies and techniques, of varying degrees of sophistication and accuracy. However, most of these efforts were aimed at systems in a given fixed geometrical configuration.

0163-1829/93/48(4)/2081(17)/$06.00

While in a full description of the energetics and dynamics of a materials system all constituents (electronic and nuclear) should be treated quantum mechanically, physical and practical considerations motivate calculations within the Born-Oppenheimer (BO) approximation,[7] which invokes a separation between the time scales for ionic and electronic motions. This restricts the dynamical evolution of the nuclear system to a single electronic potential energy surface (PES). The main task is to develop efficient and accurate methods for calculating, for a given configuration of the nuclei, the electronic energy on this PES (the ground state in our calculation), and the forces on the nuclei, which can then be used in the integration of the classical equations of motion of the nuclei, advancing them by a small time increment τ to a new configuration. Repeating the process results in a simulation of the dynamical evolution of the system on the BO PES, that is, BO dynamics.

Over the past several years several methods aimed at such simulations have been proposed. These include the Car and Parrinello (CP) method,[8] which stimulated much of the development in this area, where density-functional theory (DFT),[9] within the local-density approximation (LDA),[9] in conjunction with pseudopotentials and plane-wave expansion, are used in a generalized Lagrangian formulation leading to a dynamical simulated annealing procedure; variants of the CP method using steepest-descent[10] or conjugate-gradient[11–13] techniques for minimization of the Hohenberg-Kohn energy functional;[9] methods based on iterative techniques[14,15] such as Davison's[15] or Lanczos's[16] to solve for the lowest occupied levels of the Kohn-Sham (KS) equations;[17] and methods based on evolution of the wave functions in imaginary time, using the KS Hamiltonian in conjunction with split-propagator and fast-Fourier-transform (FFT) techniques.[18,19] While in the above studies plane waves were used, methods where other basis sets, such as Gaussians or floating Gaussians,[20] augmented-plane-wave (APW)-like schemes,[21,22] and generalized valence bond[23] are employed, have been proposed. In addition several schemes have been developed where simplified, approximate descriptions of the electronic problem are adopted, such as a pseudopotential perturbative approach,[24] tight-binding,[25] and the Harris functional[26] methods.

In this paper we describe a method for simulations of BO dynamics where the description of the electronic structure is based on LDA [or local-spin-density-functional (LSDF) theory[9] when required], in conjunction with nonlocal, norm-conserving pseudopotentials,[27] and a plane-wave basis set. Since the method was developed by us in the context of our investigations of finite aggregates (clusters),[28–31] certain aspects of it are designed for such systems (although the generalization to extended systems is rather obvious). In particular, in contrast to other BO dynamical simulations of clusters,[32] our method does not employ a supercell replication procedure, and thus no repeated images of the system are involved. This allows us to study efficiently systems possessing large multipole moments, which may become prohibitive when a supercell method is used because of the large length scale necessary for the interaction between images in periodically replicated cells to vanish. Furthermore, in our method the ground-state electronic energy and forces on the ions are calculated during a dynamical simulation for each nuclear configuration,[33] thus allowing a relatively large time step, $\tau \approx 1-10$ fs, for integration of the ionic equations of motion.

In Sec. II and the associated appendices, a detailed description of our method is given. In previous studies, we have used our method for investigations of neutral and charged metal clusters,[29] fission dynamics of charged clusters,[29] metallization of alkali-halide clusters,[28] mixed lithium-aluminum clusters,[31] solvation of sodium in water clusters,[30(a)] and dielectrons in water clusters.[30(b)]. In Sec. III, we apply the method to investigations of the energetics, structure, and dynamics of the water-dimer molecule $(H_2O)_2$, which is a prototype system for studies of the nature of hydrogen bonding. In addition to the information we obtain pertaining to the $(H_2O)_2$ molecule, this study demonstrates the applicability of our BO-dynamics simulation method for a system containing oxygen and hydrogen atoms and involving weak intermolecular hydrogen-bond interactions, which constitutes a most severe test of the accuracy of quantum-mechanical electronic-structure calculations. A summary of our results is given in Sec. IV.

II. METHOD

A. Basic theory

The total energy of a system of ions and valence electrons on the Born-Oppenheimer potential-energy surface can be written as

$$E_{\text{total}}(\{\mathbf{r}_I\},\{\dot{\mathbf{r}}_I\}) = \sum_I \tfrac{1}{2} m_I |\dot{\mathbf{r}}_I|^2 + \sum_{I>J} Z_I Z_J / |\mathbf{r}_I - \mathbf{r}_J| + E_{\text{elec}}(\{\mathbf{r}_I\}) , \quad (1)$$

where $\mathbf{r}_I$, m_I, and Z_I are the position, mass, and charge of the Ith ion, and $E_{\text{elec}}(\{\mathbf{r}_I\})$ is the ground-state energy of the valence electrons evaluated for the ionic configuration $\{\mathbf{r}_I\}$. The first two terms in Eq. (1) correspond to the ionic kinetic and interionic interaction energies, respectively.

The major task is to calculate the ground-state electronic energy which we compute via KS formulation[17] of the LSDF theory,[34] with (in the present implementation) a post-LSD gradient correction to the exchange-correlation energy[35,36] added in some instances. The ground-state energy of the valence electrons in this approximation is given by

$$E_{\text{elec}} = T_e + E_{eI} + E_{ee} , \quad (2)$$

where T_e is the kinetic energy; E_{eI} is the electron-ion interaction energy, with the interaction potential between the ions and the valence electrons described by separable norm-conserving nonlocal pseudopotentials;[27] and E_{ee} is the electron-electron interaction energy. The three terms are discussed below, and in Sec. II B our dual-space plane-wave method[37] for finite systems is described in detail.

In the KS-LSD method one solves for the wave functions $\psi_{j\sigma}$, which are eigenfunctions of a self-consistent independent-particle Schrödinger equation (the KS equation),

$$\{-\tfrac{1}{2}\nabla^2+\hat{V}_\sigma(\rho_+,\rho_-)\}\psi_{j\sigma}=\epsilon_{j\sigma}\psi_{j\sigma} , \tag{3}$$

where σ is the spin index ($\sigma=\pm$). The corresponding density for spin manifold σ is given by

$$\rho_\sigma=\sum_j f_{j\sigma}|\psi_{j\sigma}|^2 , \tag{4}$$

where $\{f_{j\sigma}\}$ are the occupation numbers, with $\sum_{j,\sigma}f_{j\sigma}=N_{\rm elec}$, and $N_{\rm elec}$ is the number of valence electrons. For a finite system, and providing the ground state is not degenerate, the lowest $N_{\rm elec}$ orbitals should be occupied; however, if the gap between occupied and unoccupied eigenvalues is very small, it may be necessary to have fractional occupation numbers to achieve self-consistency, and we use a Fermi function[19(a),38] with $k_BT\leq 0.001$ a.u. in such instances.

The KS potential operator, $\hat{V}_\sigma$ of Eq. (3), is given by the functional derivative of $E_{\rm elec}$,

$$\hat{V}_\sigma=\delta E_{\rm elec}/\delta\rho_\sigma , \tag{5}$$

and since it depends on the electronic density it must be obtained self-consistently. This is achieved by employing an iterative density-mixing scheme in the solution of Eqs. (3)–(5) as described in Appendix A. The lowest n_s ($n_s\geq N_{\rm elec}$) eigenfunctions of the KS equation for a given $\hat{V}_\sigma$ are obtained by an iterative diagonalization method similar to the "Block-Davidson" method,[14,15] which we have developed and describe in Appendix B.

We turn next to a description of the contributions to the ground-state energy of the valence electrons, Eq. (2), and the KS potential, Eq. (5).

(1) T_e is the kinetic energy of the independent-particle KS wave functions, given by

$$T_e=\sum_{j,\sigma}f_{j\sigma}\langle j\sigma|\hat{T}|j\sigma\rangle , \tag{6}$$

where the kinetic-energy operator $\hat{T}=-\frac{1}{2}\nabla^2$ is diagonal in momentum space. In our dual-space plane-wave method this term is evaluated in momentum space [see Sec. II B 1, Eq. (24b)].

(2) The electron-ion interaction is treated via separable nonlocal pseudopotentials,[27]

$$E_{eI}=\sum_{j,\sigma}f_{j\sigma}\sum_I\langle j\sigma|\hat{V}_I|j\sigma\rangle , \tag{7}$$

where in real space

$$V_I(\mathbf{r}_I;\mathbf{r},\mathbf{r}')=V_I^{\rm lc}(|\mathbf{r}-\mathbf{r}_I|)\delta(\mathbf{r}-\mathbf{r}')+V_I^{\rm nlc}(\mathbf{r}-\mathbf{r}_I,\mathbf{r}'-\mathbf{r}_I) . \tag{8}$$

The nonlocal term (for an ion at the origin) is obtained from a semilocal pseudopotential via the Kleinman-Bylander prescription:[39]

$$V_I^{\rm nlc}(\mathbf{r},\mathbf{r}')=\sum_{l,m}F_l^IK_{lm}^I(\mathbf{r})K_{lm}^I(\mathbf{r}') , \tag{9}$$

where

$$K_{lm}^I(\mathbf{r})=\Delta V_l^I(r)R_l^I(r)Y_{lm}(\hat{r}) , \tag{10}$$

and

$$F_l^I=\left[\int_0^\infty dr[rR_l^I(r)]^2\Delta V_l^I(r)\right]^{-1} , \tag{11}$$

where $\Delta V_l^I(r)$ and $R_l^I(r)$ are the semilocal pseudopotential and radial pseudowave function, respectively.

For the purpose of determining the Kohn-Sham potential operator, Eq. (5), it is convenient to separate E_{eI} into local and nonlocal parts:

$$E_{eI}^{\rm lc}=\int d^3r[\rho_+(\mathbf{r})+\rho_-(\mathbf{r})]\sum_I V_I^{\rm lc}(|\mathbf{r}-\mathbf{r}_I|) , \tag{12a}$$

and

$$E_{eI}^{\rm nlc}=\sum_{j,\sigma}f_{j\sigma}\sum_{I,l,m}F_l^I\left|\int d^3rK_{lm}^I(\mathbf{r}-\mathbf{r}_I)\psi_{j\sigma}(\mathbf{r})\right|^2 . \tag{12b}$$

The local contribution to $\hat{V}_\sigma$ is given by

$$V_{eI}^{\rm lc}(\mathbf{r})=\frac{\delta E_{\rm el}^{\rm lc}}{\delta\rho_\sigma(\mathbf{r})}=\sum_I V_I^{\rm lc}(|\mathbf{r}-\mathbf{r}_I|) , \tag{13a}$$

and can be combined with the LSD potential (see below). The nonlocal KS potential is

$$V_{eI}^{\rm nlc}(\mathbf{r},\mathbf{r}')=\sum_I V_I^{\rm nlc}(\mathbf{r}-\mathbf{r}_I,\mathbf{r}'-\mathbf{r}_I) , \tag{13b}$$

where $V_I^{\rm nlc}$ is given by Eqs. (9)–(11).

(3) The electron-electron many-body interaction is given by

$$E_{ee}=\int d^3r[\rho_+(r)+\rho_-(r)][\epsilon_H(\mathbf{r})+\epsilon_{\rm xc}(\mathbf{r})] , \tag{14}$$

where

$$\epsilon_H(\mathbf{r})=\tfrac{1}{2}\int d^3r'[\rho_+(\mathbf{r}')+\rho_-(\mathbf{r}')]/|\mathbf{r}-\mathbf{r}'| , \tag{15}$$

is the "Hartree" energy functional, and

$$\epsilon_{\rm xc}(\mathbf{r})=e_{\rm xc}[\rho_+(\mathbf{r}),\rho_-(\mathbf{r});\nabla\rho_+(\mathbf{r}),\nabla\rho_-(\mathbf{r})] , \tag{16}$$

is the exchange-correlation energy functional. In LSD, $e_{\rm xc}$ depends only on the densities and is simply the exchange-correlation energy per electron of a uniform electron gas with densities $\rho_+(\mathbf{r})$ and $\rho_-(\mathbf{r})$; in our calculations we use the Vosko-Wilks[40] parameterization of the Ceperly-Alder[41] result. If a gradient correction is added, then $e_{\rm xc}$ also depends on the density gradients, $\nabla\rho_+(\mathbf{r})$ and $\nabla\rho_-(\mathbf{r})$. We have used the exchange-gradient correction of Becke[35(a)] and the correlation-gradient correction of Perdew[36] in the post-LSD approximation; that is, we calculate the gradient correction to the energy non-self-consistently using the (self-consistent) KS-LSD-generated density. This approach has been shown to be justified via calculations for a number of molecules.[42] However, the geometries obtained by minimizing the energy on the (non-gradient-corrected) LSD potential-energy surface may be in error, particularly for hydrogen-bonded systems (as found in our work,[30(a)] and Sec. III of this paper, as well as in Ref. 43).

Finally, the contribution of the electron-electron in-

teraction to the KS potential at the LSD level is given by

$$V_\sigma^{\rm LSD}(\mathbf{r})=\frac{\delta E_{ee}}{\delta\rho_\sigma(\mathbf{r})}=2\epsilon_H(\mathbf{r})+\left[1+\rho_\sigma(\mathbf{r})\frac{\partial}{\partial\rho_\sigma(\mathbf{r})}\right]\times e_{\rm xc}[\rho_+(\mathbf{r}),\rho_-(\mathbf{r})]\ , \tag{17}$$

where $\epsilon_H(\mathbf{r})$ is given by Eq. (15) and $e_{\rm xc}$ and its derivatives are given in Ref. 40. The gradient-correction contributions to the potential have also been published.[35,36,42]

B. A dual-space plane-wave method for finite systems

In this section we discuss in detail our use of the plane-wave basis set in the calculation of the ground state of the electronic energy of a finite (nonperiodic) system. Our method is a dual-space method (both real- and momentum-space representations of the wave functions are used), similar to that developed for band-structure calculations and *ab initio* molecular dynamics with periodic boundary conditions.[33,37] We emphasize, however, that while we use a plane-wave basis set for finite systems, we do not employ a supercell procedure, i.e., there are no periodically repeated images of the system. The advantage of this approach is that it enables us to treat systems that have large multipole moments, avoiding the need for the large-length scale that would be necessary in a supercell method to make the interaction with images negligible (see Sec. III).

1. Plane-wave expansion of the wave functions

We define a calculational cell to be the region of space given by

$$\mathbf{r}\equiv(x,y,z);\quad 0\le x<L_x,\quad 0\le y<L_y,\quad 0\le z<L_z\ . \tag{18}$$

The wave function $\psi_{j\sigma}(\mathbf{r})=\langle\mathbf{r}|j\sigma\rangle$ is expanded in a plane-wave basis *within* the cell, i.e.,

$$\psi_{j\sigma}(\mathbf{r})=\Omega^{-1/2}\sum_{\mathbf{g}}\tilde{\phi}_{j\sigma}(\mathbf{g})e^{i\mathbf{g}\cdot\mathbf{r}} \tag{19a}$$

for $\mathbf{r}$ in the cell, and

$$\psi_{j\sigma}(\mathbf{r})=0 \tag{19b}$$

for $\mathbf{r}$ *outside* the cell.

In Eq. (19a) Ω is the volume of the cell, $\Omega=L_xL_yL_z$, and $\tilde{\phi}_{j\sigma}(\mathbf{g})$ are the coefficients of the plane-wave expansion. The reciprocal-space (g-space) grid is defined by

$$\mathbf{g}=2\pi(k_x/L_x,k_y/L_y,k_z/L_z)\ , \tag{20a}$$

where $k_\alpha(\alpha=x,y,z)$ are integers satisfying

$$-N_\alpha/2\le k_\alpha\le N_\alpha/2\ . \tag{20b}$$

The sum over $\mathbf{g}$ in Eq. (19a) includes all combinations of (k_x,k_y,k_z) satisfying Eq. (20b). We note that while the wave function is *defined* to be zero outside the cell, its amplitude $\psi_{j\sigma}(\mathbf{r})$ and gradient $\nabla\psi_{j\sigma}(\mathbf{r})$ are required to vanish (or be negligibly small) on the boundary of the cell. For a finite system this condition can be satisfied by increasing the dimensions of the calculational cell $\{L_\alpha\}$ and/or by translating and rotating the system inside the cell. The L_α need not be equal (i.e., the cell need not be a cube). In most circumstances we choose the lengths $\{L_\alpha\}$ and the integers $\{N_\alpha\}$ Eq. (20b) such that $N_x/L_x=N_y/L_y=N_z/L_z=g_{\rm max}/\pi$ and impose a spherical momentum cutoff, that is,

$$\tilde{\phi}_{j\sigma}(\mathbf{g})=0\ \text{ for }|\mathbf{g}|>g_{\rm max}\ . \tag{21}$$

The choice of the momentum cutoff $g_{\rm max}$ is dictated primarily by the nature of the ionic pseudopotentials while the lengths $\{L_\alpha\}$ are determined by the physical size and geometry of the system. Together these determine the number of plane waves $N=N_xN_yN_z$.

Since we are dealing with eigenfunctions of a finite nonperiodic system, we can require, without loss of generality, that the wave functions be real in real space, i.e.,

$$\psi_{j\sigma}(\mathbf{r})=\psi_{j\sigma}^*(\mathbf{r})\ \text{ and }\ \tilde{\phi}_{j\sigma}(\mathbf{g})=\tilde{\phi}_{j\sigma}^*(-\mathbf{g})\ . \tag{22}$$

Orthonormality of the wave functions gives

$$\langle j\sigma|j'\sigma\rangle=\sum_{\mathbf{g}}\tilde{\phi}_{j\sigma}(-\mathbf{g})\tilde{\phi}_{j'\sigma}(\mathbf{g})=\delta_{jj'}\ . \tag{23}$$

In the dual-space method, the gradient operator is diagonal in the plane-wave basis,

$$\nabla\psi_{j\sigma}(\mathbf{r})=\Omega^{-1/2}\sum_{\mathbf{g}}i\mathbf{g}\tilde{\phi}_{j\sigma}(\mathbf{g})e^{i\mathbf{g}\cdot\mathbf{r}}\ , \tag{24a}$$

and

$$\langle j\sigma|-\tfrac{1}{2}\nabla^2|j'\sigma\rangle=\tfrac{1}{2}\sum_{\mathbf{g}}g^2\tilde{\phi}_{j\sigma}(-\mathbf{g})\tilde{\phi}_{j'\sigma}(\mathbf{g})\ . \tag{24b}$$

2. Plane-wave expansion of the density and the real-space grid

The density $\rho_\sigma(\mathbf{r})$ can also be expanded in a Fourier series but requires a momentum cutoff which is twice as large as that of the wave functions. This expansion is useful in evaluating the gradient corrections to the LSD, and in motivating our treatment of the potential operators in real space (see Secs. II B 3 and II B 4 below). Thus, we write

$$\rho_\sigma(\mathbf{r})=\Omega^{-1}\sum_{\mathbf{g}}\sum_{\mathbf{g}'}\left[\sum_j f_{j\sigma}\tilde{\phi}_{j\sigma}(-\mathbf{g})\tilde{\phi}_{j\sigma}(\mathbf{g}')\right]e^{i(\mathbf{g}-\mathbf{g}')\cdot\mathbf{r}}=\Omega^{-1}\sum_{\mathbf{G}}\tilde{D}_\sigma(\mathbf{G})e^{i\mathbf{G}\cdot\mathbf{r}}\ . \tag{25}$$

The "G-space" grid in Eq. (25) is defined as

$$\mathbf{G}=2\pi(m_x/L_x,m_y/L_y,m_z/L_z)\ , \tag{26a}$$

where m_α $(\alpha=x,y,z)$ are integers satisfying

$$-M_\alpha/2\le m_\alpha\le M_\alpha/2\ \text{ and }\ M_\alpha=2N_\alpha\ . \tag{26b}$$

Now the gradient, $\nabla\rho_\sigma(\mathbf{r})$, which is needed for evaluation of the exchange-correlation gradient corrections, is given by

$$\nabla\rho_\sigma(\mathbf{r})=\Omega^{-1}\sum_{\mathbf{G}}i\mathbf{G}\tilde{D}_\sigma(\mathbf{G})e^{i\mathbf{G}\cdot\mathbf{r}}\ . \tag{27}$$

The coefficients $\tilde{D}_\sigma(\mathbf{G})$ can be evaluated directly from the wave-function coefficients $[\tilde{\phi}_{j\sigma}]$ [see Eq. (25)]. A more efficient method is to evaluate $\rho_\sigma(\mathbf{r})$ on a real-space grid which is the dual of the G-space grid, and use a discrete Fourier transform, i.e., FFT, to get $\tilde{D}_\sigma(\mathbf{G})$. We define the real-space grid, the "S grid," as

$$\mathbf{S}=(n_x L_x/M_x, n_y L_y/M_y, n_z L_z/M_z) , \tag{28}$$

where n_α are integers satisfying $0 \le n_\alpha \le M_\alpha - 1$. The density on the S grid is defined as

$$D_\sigma(\mathbf{S})=(\Omega/M)\rho_\sigma(\mathbf{S}) , \tag{29}$$

where $M=M_x M_y M_z$ is the number of real-space grid points, and the set $[D_\sigma(\mathbf{S})]$ is the "FFT dual" of $[\tilde{D}_\sigma(\mathbf{G})]$,

$$\tilde{D}_\sigma(\mathbf{G})=M^{-1/2}\sum_{\mathbf{S}} D_\sigma(\mathbf{S})e^{-i\mathbf{G}\cdot\mathbf{S}} . \tag{30}$$

In order to obtain $\{D_\sigma(\mathbf{S})\}$ we define the wave function on the S grid,

$$\phi_{j\sigma}(\mathbf{S})=(\Omega/M)^{1/2}\psi_{j\sigma}(\mathbf{S}) \tag{31}$$

or, in terms of plane-wave coefficients,

$$\phi_{j\sigma}(\mathbf{S})=M^{-1/2}\sum_{\mathbf{g}} \tilde{\phi}_{j\sigma}(\mathbf{g})e^{i\mathbf{g}\cdot\mathbf{S}} , \tag{32}$$

where the coefficients $D_\sigma(\mathbf{S})$ are given by

$$D_\sigma(\mathbf{S})=\sum_j f_{j\sigma}|\phi_{j\sigma}(\mathbf{S})|^2 . \tag{33}$$

We note here that the wave function on the S grid, $[\phi_{j\sigma}(\mathbf{S})]$ in Eq. (32), is *not* the FFT dual of the plane-wave coefficients, $\{\tilde{\phi}_{j\sigma}(\mathbf{g})\}$. There are several methods for obtaining $[\phi_{j\sigma}(\mathbf{S})]$ from $\{\tilde{\phi}_{j\sigma}(\mathbf{g})\}$ using standard FFT routines (two such methods are described in Appendix C).

3. *Terms which are local in real space*

Potential-energy terms that involve real-space integrals over the density, such as $E_{eI}^{\rm lc}$, Eq. (12a), and E_{ee}, Eq. (14), are evaluated via sums on the S grid. Such terms are of the form

$$E[\rho_\sigma,\epsilon]=\int d^3r\,\rho_\sigma(\mathbf{r})\epsilon(\mathbf{r}) . \tag{34}$$

Defining

$$\tilde{e}(\mathbf{G})=\Omega^{-1}\int_0^{L_x}dx\int_0^{p}l_y dy\int_0^{L_z}dz\,\epsilon(\mathbf{r})e^{-i\mathbf{G}\cdot\mathbf{r}} , \tag{35a}$$

and

$$e(\mathbf{S})=\sum_{\mathbf{G}}\tilde{e}(\mathbf{G})e^{i\mathbf{G}\cdot\mathbf{S}} , \tag{35b}$$

$E[\rho_\sigma,\epsilon]$ of Eq. (34) can be expressed, without approximation, as

$$E[\rho_\sigma,\epsilon]=\sum_{\mathbf{S}} D_\sigma(\mathbf{S})e(\mathbf{S}) . \tag{36}$$

Obviously, there is little advantage to this if we must evaluate the integrals in Eq. (35a) to calculate $\tilde{e}(\mathbf{G})$. In the case that periodic boundary conditions are employed, many (but not all) of the terms corresponding to $\tilde{e}(\mathbf{G})$ could be easily evaluated; for instance, the sum over local pseudopotentials could be expressed as a product of the Fourier-transformed pseudopotential and the structure factor associated with the ionic configuration within the periodically repeated cell.[36] The approximation we make in the current version of our method is

$$e(\mathbf{S})\cong\epsilon(\mathbf{S}) , \tag{37}$$

which is equivalent to a "rectangle rule" for the numerical integration of the integrals in Eq. (34) or (35a). This approximation is most satisfactory when the solution, i.e., the energy $E_{\rm elec}$, Eq. (2) is converged with respect to increasing the plane-wave momentum cutoff $g_{\max}$, Eq. (21); but for too small a value of $g_{\max}$ the solution will depend on the origin and orientation of the real-space S grid. We have attempted to reduce the S-grid spacing (while keeping $g_{\max}$ constant) by replacing M_α in Eq. (26b) with $M_\alpha=mN_\alpha$, $m>2$; however, we found that better results were obtained for the same computational effort by increasing the momentum cutoff $g_{\max}$ (which also reduces the real-space grid spacing).

To summarize the treatment of terms local in real space: (i) The wave functions, Eq. (32), and the density and its gradient, Eqs. (33) and (27), are evaluated on the real-space grid defined by Eqs. (28) (the S grid); (ii) the subsequent evaluation of the local-energy terms on the S grid, with the exception of the Hartree term, Eq. (15), is straightforward and requires no further explanation. Evaluation of the Hartree term is discussed in Appendix D.

4. *Separable nonlocal pseudopotential*

Evaluation of matrix elements of the separable nonlocal pseudopotential, Eqs. (9)–(11), requires calculation of an integral involving the wave function [see Eq. (12b)], which can be done most efficiently in real space since the semilocal pseudopotential $\Delta V_l^I(r)=0$ for $r>r_c$, and thus the integral in real space need not be over all space. We approach this task in a manner similar to our treatment of the local terms. Define

$$B_{lm}^I(\mathbf{S})=\sum_{\mathbf{G}}\int_0^{L_x}dx\int_0^{L_y}dy\int_0^{L_z}dz\,K_{lm}^I(\mathbf{r}-\mathbf{r}_I)e^{i\mathbf{G}\cdot(\mathbf{S}-\mathbf{r})} , \tag{38}$$

then without approximation

$$\sum_{\mathbf{S}} B_{lm}^I(\mathbf{S})\phi_{j\sigma}(\mathbf{S})=\int d^3r\,K_{lm}^I(\mathbf{r}-\mathbf{r}_I)\psi_{j\sigma}(\mathbf{r}) . \tag{39}$$

We now make the approximation [see also Eq. (37)]

$$B_{lm}^I(\mathbf{S})\cong K_{lm}^I(\mathbf{S}-\mathbf{r}_I) . \tag{40}$$

In principle, the sum in Eq. (39) could be performed on a real-space grid which is the dual of the reciprocal-space g grid; however, since we have already made use of the wave functions represented on the $\mathbf{S}$ grid, $\{\phi_{j\sigma}(\mathbf{S})\}$ in the evaluation of the local terms, we use the S grid here as well. King-Smith, Payne, and Lin[44] have given a pro-

cedure for improving on the ansatz of Eq. (40). We found that in all cases we have tried, the error associated with Eq. (40) is smaller than that due to the ansatz in Eq. (37), and that the two tend to cancel.

5. *Hamiltonian matrix elements:* $\langle \mathbf{g}|H|j\sigma\rangle$

In our procedure for solving for the eigenfunctions of the KS equation (see Appendix B), all calculations are done with the momentum-space representation of the wave functions except for the $\hat{V}_\sigma\psi_{j\sigma}$ operation, which is performed in real space. In the previous sections (3 and 4) we have described the calculation of terms in the expression for the energy, Eqs. (12) and (14). Using the notation of the preceding sections, we now provide expressions for the various terms arising in the course of calculating the operation of the KS Hamiltonian on a wave function. We define

$$\psi'_{j\sigma}=\hat{H}\psi_{j\sigma}\ , \tag{41a}$$

and the g-grid transform [see Eq. (20)]

$$\psi'_{j\sigma}(\mathbf{r})=\sum_{\mathbf{g}}\tilde{\phi}'_{j\sigma}(\mathbf{g})e^{i\mathbf{g}\cdot\mathbf{r}}\ . \tag{41b}$$

Using Eqs. (41), the Hamiltonian matrix element is given by

$$\langle j\sigma|\hat{H}|k\sigma\rangle=\sum_{\mathbf{g}}\tilde{\phi}_{j\sigma}(-\mathbf{g})\tilde{\phi}'_{k\sigma}(\mathbf{g})\ . \tag{42}$$

Combining our results, the plane-wave coefficients $\tilde{\phi}'_{j\sigma}(\mathbf{g})=\Omega^{1/2}\langle \mathbf{g}|\hat{H}|j\sigma\rangle$ are given by

$$\tilde{\phi}'_{j\sigma}(\mathbf{g})=\tfrac{1}{2}g^2\tilde{\phi}_{j\sigma}(\mathbf{g})+M^{-1/2}\sum_{\mathbf{S}}\left[[V_\sigma^{\mathrm{LSD}}(\mathbf{S})+\sum_I V_I^{\mathrm{lc}}(|\mathbf{S}-\mathbf{r}_I|)]\phi_{j\sigma}(\mathbf{S})+\sum_I\sum_{l,m}F_l^I K_{lm}^I(\mathbf{S}-\mathbf{r}_I)\sum_{\mathbf{S}'}K_{lm}^I(\mathbf{S}'-\mathbf{r}_I)\phi_{j\sigma}(\mathbf{S}')\right]e^{-i\mathbf{g}\cdot\mathbf{S}}\ . \tag{43}$$

6. *Forces*

Calculations involving classical dynamics of the ions on the ground-state BO electronic potential-energy surface (that is, Born-Oppenheimer dynamics, BO-LSD-MD) require evaluation of the force on each ion due to its interaction with the ground-state electronic density. These forces can be evaluated straightforwardly via the Hellman-Feynman theorem[45] (there are no basis-set corrections) by taking the gradients of the Hamiltonian matrix elements with respect to the ionic positions $\{\mathbf{r}_I\}$. While this may be easily achieved using Eqs. (42) and (43), the calculation can be performed more efficiently in real space, and the local pseudopotential contribution can be expressed in terms of the density. The resulting expression is given by

$$\nabla_{\mathbf{r}_I}E_{eI}=\sum_{\mathbf{S}}[D_+(\mathbf{S})+D_-(\mathbf{S})]\sum_I\nabla_{\mathbf{r}_I}V_I^{\mathrm{lc}}(|\mathbf{S}-\mathbf{r}_I|)+2\sum_{j,\sigma}f_{j\sigma}\sum_I\sum_{l,m}F_l^I\left[\sum_{\mathbf{S}}\phi_{j\sigma}(\mathbf{S})K_{lm}^I(\mathbf{S}-\mathbf{r}_I)\sum_{\mathbf{S}'}\nabla_{\mathbf{r}_I}K_{lm}^I(\mathbf{S}'-\mathbf{r}_I)\phi_{j\sigma}(\mathbf{S}')\right]\ . \tag{44}$$

The electronic force obtained via Eq. (44), together with the interionic Coulomb repulsion, governs the nuclear dynamical evolution generated via integration of the Newtonian equations of motion

$$m_I\ddot{\mathbf{r}}_I=-\nabla_{\mathbf{r}_I}E_{eI}(\{\mathbf{r}_I\})-\nabla_{\mathbf{r}_I}\left[\sum_{I>J}Z_IZ_J/|\mathbf{r}_I-\mathbf{r}_J|\right]\ . \tag{45}$$

In our simulations the integration is performed using the Gear fifth-order predictor-corrector algorithm[1] with a time step of the order of 1–10 fs, depending on the characteristic frequencies of the classical degrees of freedom.

III. CASE STUDY: H_2O AND $(H_2O)_2$

Previous applications of the method outlined in Sec. II (or earlier versions of the method) have been made by us to a variety of problems, including neutral and ionized alkali,[29] alkali-halide,[28] and lithium-aluminum[31] clusters. Most recently, we have used the method to investigate the structure and energetics of $Na(H_2O)_n$ $(1\le n\le 8)$ clusters.[30(a)] To illustrate the method we apply it here to calculations of energetics and dynamics of the water molecular dimer $(H_2O)_2$. This system was chosen because it has been extensively investigated both experimentally and theoretically (see reviews and literature citations in Refs. 46–53) and because it illustrates the ability to treat both chemical bonds, i.e., the H_2O molecule, and the much weaker intermolecular hydrogen-bond interaction in the dimer. Furthermore, our investigation of this system demonstrates also the ability to treat finite systems with large multipole moments; we estimate that to obtain comparable accuracy for the water dimer with a supercell method one would have to more than double the linear dimensions of the calculational cell, which would increase the number of plane waves by a factor of at least eight for the same plane-wave energy cutoff E_{pwc}.

A. Calculational details

In our calculations we have used pseudopotentials (PP) generated by the method of Troullier and Martins.[27] For oxygen we have used p-local and s-nonlocal PP's, both with a core radius of $1.45a_0$. Previous studies[54] of the crystalline properties of SiO_2 and TiO_2 using this PP for oxygen yielded converged results for the total energy, with $E_{\rm pwc} \gtrsim 70$ Ry. For hydrogen, we have used an s-local pseudopotential with a core radius of $0.95a_0$. In our calculations the nuclei are treated classically. While this is common practice in theoretical structural studies and molecular-dynamics simulations of water and other hydrogen-containing molecules, in a more rigorous treatment quantum effects associated with the light-mass protons should be considered.

To examine convergence we have calculated the total, atomization, and binding energies for a rigid geometry of $(H_2O)_2$, using various plane-wave cutoff energies $E_{\rm pwc}$. We found that, compared with calculations using a very large value of $E_{\rm pwc}=217$ Ry, using $E_{\rm pwc}=96$ Ry yielded results that differed by 0.08 a.u. (0.2%), 0.02 a.u. (2.3%), and 0.0005 a.u. (3.4%) for the total, atomization, and dimer binding energies, respectively, while calculations using an even smaller value of $E_{\rm pwc}=62$ Ry yielded differences that were about twice as large. When minimizing the energy (i.e., optimizing the structure of the dimer molecule) we found that the differences between calculations with $E_{\rm pwc}=62$ Ry and results obtained with $E_{\rm pwc}=96$ Ry for the atomization and binding energy were 0.015 a.u. (1.7%) and 0.0002 a.u. (1.4%), respectively, (see Tables I and II). For calculations of the monomer, we used a cubic calculational cell with an edge length of $15a_0$, while for the dimer $(H_2O)_2$ molecule cell dimensions of $15a_0\times15a_0\times20a_0$ were used. In dynamical BO-LSD-MD simulations a time step $\tau=0.4$ fs was used in the integration of the equations of motion of the nuclei, and the total energy of the system was conserved to better than 3×10^{-5} a.u. (10^{-4}% of the total energy), throughout our dynamical simulations.

B. Structure and vibrational frequencies

(i) *Water monomer H_2O.* To investigate the ground-state structure and dynamics of the water molecule we performed comparative energy minimization and finite temperature ($T=150$ K) MD simulations, using $E_{\rm pwc}=62$ and 96 Ry. The results of these calculations are summarized in Table I. The vibrational frequencies were obtained from the Fourier transform of the velocity correlation functions generated by the MD simulation. Also included in Table I are the APW results of Soler and Williams[21(b)] and the results of Sim *et al.*[49] using a localized basis set (LCGTO) (LDA was used in both calculations).

As expected, the calculated atomization energy, ΔE_a, is overestimated in these calculations, which is a common finding in calculations using local-density functionals. However, we note that this may be partially corrected by a post-LSD gradient correction [compare ΔE_a and ΔE_a(xcg) in Table I]. Our results for structure, dipole moment (μ), polarization (α), and vibrational frequencies of the H_2O molecule compare very well with experiment and with the other two LSD-based calculations. The frequencies obtained by the LCGTO-LSD method are somewhat closer to experiment than ours; however, these were obtained from a force-constant matrix, whereas, as mentioned above, we have determined them from a finite-temperature simulation.

(ii) Water dimer $(H_2O)_2$. The nature of the hydrogen bonding in small clusters, and in condensed phases, has been the subject of extensive experimental and theoretical investigations (see Refs. 46–53 and citations therein). In particular, among all intermolecular hydrogen-bonded systems the water dimer is the best studied because of the key role it plays in understanding the properties of liquid

TABLE I. Calculated and experimentally measured atomization energy ΔE_a (in units of kcal/mol), structural parameters (distance in Å, angle in degrees), dipole moment μ (in unit of Debye), polarizability α (in a.u.), and vibrational frequencies ν (in units of cm^{-1}) for the equilibrium structure of a water monomer. Results using our methods are given for two plane-wave cutoff energies $E_{\rm pwc}=62$ Ry and 96 Ry. For the atomization energy, results including post-LSD exchange-correlation gradient corrections are denoted by ΔE_a(xcg).

	$E_{\rm pwc}=62$ Ry	$E_{\rm pwc}=96$ Ry	APW[a]	LCGTO[b]	exp[c]
ΔE_a	273.5	268.7	267.0		219.3
ΔE_a(xcg)	249.1	244.2			219.3
r(OH)	0.956	0.960	0.968	0.978	0.9572
ϕ(HOH)	107.4	105.5	102.4	104.4	104.52
μ	1.670	1.686		2.026	1.855
α		10.3			9.6
ν_1	3713	3740	3600	3705	3657
ν_2	1575	1550	1610	1562	1595
ν_3	3944	3840	3670	3809	3756

[a]Reference 21b.
[b]"VWN" results in Ref. 49.
[c]Experimental results compiled in Ref. 49.

water.

Hydrogen bond energies are of the order of a few kcal/mol, which lie between typical values associated with dispersion interactions and those corresponding to true chemical bonds. Consequently, quantitative quantum-mechanical calculations of the interaction energy in the dimer molecule, obtained as the difference between the dimer energy and twice the monomer energy, are most difficult, exhibiting sensitivity to the basis set used, basis-set extension effects (BSE) and in particular to basis set superposition errors (BSSE).[48,50,55] Therefore, calculations of energetics and dynamics of this system, using the method described in Sec. II, which is based on density-functional theory, provide a most stringent test of the accuracy that can be obtained by the method.

Our results for the minimum-energy structure, dipole moment, and vibrational frequencies of the water dimer are summarized in Table II, along with the LCGTO results of Sim *et al.*[49] and those obtained from experimental data. [The equilibrium structure of $(H_2O)_2$ and definitions of structural parameters are shown in Fig. 1.] As is evident from inspection of Table II, our results are in good agreement with experiment. As has been noted previously, in LSD calculations the binding energy is overestimated and the hydrogen-bond distance in the equilibrium geometry is too small (the O-O distance is about 10% too small). To correct for these discrepancies we have applied a post-LSD exchange-correlation gradient correction (xcg) and minimized the energy with respect to the interoxygen distance, keeping other

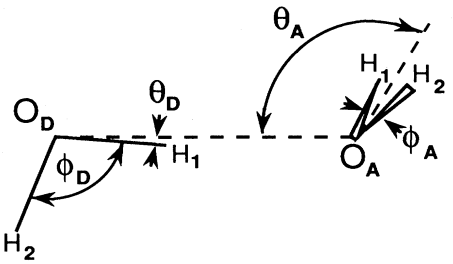

FIG. 1. Schematic drawing of the equilibrium structure of the hydrogen-bonded $(H_2O)_2$ molecule. O_D and O_A denote the oxygen atoms of the donor and acceptor molecules, respectively. The donor molecule is in the plane, and the plane of the acceptor molecule, defined by $H_1O_AH_2$, is normal to the plane of the paper. Geometrical parameters defining the structure are denoted as outlined in Table II.

TABLE II. Calculated and experimentally measured binding energy ΔE_b (in kcal/mol), structural parameters (distances in Å, and angles in degree), dipole moment μ (in units of Debye), polarizability α (in a.u.), and vibrational frequencies ν (in cm^{-1}) for the equilibrium structure of a water dimer. The oxygens of the water molecules in the dimer are denoted as O_A and O_D, corresponding to the acceptor and donor molecules, respectively, and H_1 is the hydrogen atom of the donor molecule bridging it [i.e., hydrogen bonding to the acceptor molecule (see Fig. 1)]. The intramolecular modes of the donor and acceptor molecules are denoted as $\nu_j(D)$ and $\nu_j(A)$, $j=1,2,3$ and the dimer intermolecular modes are denoted as ν_j $(j=7-12)$, after Ref. 49. Results of our calculations, including post-LSD exchange-correlation gradient corrections, are given in parentheses, and those in parentheses under LCGTO correspond to calculations with self-consistent inclusion of such corrections.

	$E_{pwc}=62$ Ry	$E_{pwc}=96$ Ry	LCGTO[a]	exp[b]
ΔE_b	9.19(4.91)	9.06(4.90)	9.16(4.51)	5.44±0.7
$r(O_AH)$	0.957	0.961	0.980	
$\phi_A(HO_AH)$	106.2	106.2	104.7	
$r(O_DH_1)$	0.971	0.980	0.997	
$r(O_DH_2)$	0.957	0.961	0.977	
$\phi_D(HO_DH)$	108.3	106.1	105.4	
$r(O_AO_D)$	2.68(2.96)	2.70(2.98)	2.71(2.89)	2.98±0.01
θ_A	119.8	120.6	106.0	123±10
θ_D	3.67	4.84	9.0	6±20
μ	2.56	2.57	2.39	2.60
α		20.84		
$\nu_3(A)$		3860	3786	3714
$\nu_3(D)$		3825	3744	3698
$\nu_1(A)$		3750	3686	3626
$\nu_1(D)$		3580	3394	3548
$\nu_2(D)$		1590	1574	1618
$\nu_2(A)$		1565	1563	1600
ν_7		710	785	520
ν_8		410	464	320
ν_9(O-O)		225	271	243
ν_{10}		150	174	
ν_{11}		150	163	155
ν_{12}		150	151	

[a]Reference 49, "VWN" results, and "BP" results in parentheses.

[b]Experimental results compiled in Ref. 49.

structural parameters fixed. As is evident (see results shown in parentheses in Table II), the correspondence between the calculated values and the experimental ones is significantly improved. In this context we remark that Sim *et al.*[49] have included the gradient corrections self-consistently and fully minimized the energy. They, too, found improvement in the hydrogen-bond distance and energy upon inclusion of gxc corrections, and that other structural parameters are hardly influenced by these corrections (the latter justifies our post-LSD xcg correction).

Early quantum-chemical studies[56] of the nature of bonding and structure of the water dimer have shown that while the contribution of purely electrostatic interactions (that is, the interaction between the unmodified, frozen, monomer charge densities) is large, it is essential to consider other contributions to the interaction energy, such as those originating from mixing of the occupied orbitals, the Pauli exclusion principle, polarization effects, charge transfer (that is, mixing of vacant orbitals of one partner and the occupied orbitals of the other partner), and a contribution associated with a measure of nonseparability of the hydrogen-bond energy into the individual components listed above.

The intrinsic nature of the hydrogen-bond in $(H_2O)_2$ is portrayed in the difference isodensity contour plots, shown in Fig. 2, where density-difference maps $\Delta\rho=\rho[(H_2O)_2]-2\rho(H_2O)$ obtained via our calculations are given. From these results, it is readily observed that the electron density in the region about the hydrogen of the donor molecule, bridging between it and the acceptor molecule, is reduced (i.e., the partial charge on the donor hydrogen becomes "more positive" in the dimer, compared to the isolated monomer). On the other hand, regions about the other hydrogen of the donor and close to the donor oxygen acquire some excess electron density in the dimer molecule. These results correlate with population analysis of the dimer electronic distribution,[57] indicating electron transfer ($0.02e^- - 0.03e^-$) from the proton acceptor molecule to the donor molecule.

The rearrangement of the electronic charge distribution in the dimer is reflected also in the magnitudes of the dipole moment and polarizability of $(H_2O)_2$ (see Table II). We note that the calculated magnitude of the dipole $\mu(H_2O)_2=2.57D$ (see Table II, $E_{pwc}=96$ Ry), which is close to the experimentally measured value, is significantly enhanced compared to the total dipole ($1.75D$) obtained as a vector sum of the dipoles of the individual monomers positioned in the equilibrium geometry of the dimer. In addition, the predicted polarizability $\alpha(H_2O)_2=20.84$ a.u. (see Table II) is slightly larger than $2\alpha(H_2O)=20.6$ a.u. (see Table I).

As mentioned, our calculated structural parameters for the dimer are in agreement with experimentally determined ones and the trends of changes in the monomer geometries upon formation of the dimer agree with those obtained from other calculations [i.e., widening of the HOH angle and, in particular, the increase in $r(O_DH_1)=0.980$ Å, the distance between the oxygen of the donor molecule and the bridging hydrogen, compared to $r(OH)=0.960$ Å in the monomer].

The vibrational frequencies we report in Table II were obtained from a constant energy MD simulation of 1.2-ps duration. The Fourier-transformed velocity correlation functions for the donor and acceptor molecules in the dimer are shown in Fig. 3. Due to the finite duration of the simulation, we have used a Gaussian smoothing procedure, giving a resolution of $\sigma=25$ cm^{-1}. In addition, there is broadening due to coupling between modes, particularly for the donor intramolecular modes and the low-frequency intermolecular modes. Consequently, we are unable to resolve all twelve modes from our results. Most likely, the unresolved modes are located under the lowest peak in Fig. 3 at ~ 150 cm^{-1}. The intramolecular bend (ν_2) and strength (ν_1 and ν_3) modes are labeled ($\nu_j(A)$, $\nu_j(D)$, $j=1,2,3$ for the acceptor and donor molecules, respectively. The negative shift of the donor vibrational frequencies (with respect to acceptor) is in reasonable agreement with experiment and other calculations; however, we observe an overall small positive, rather

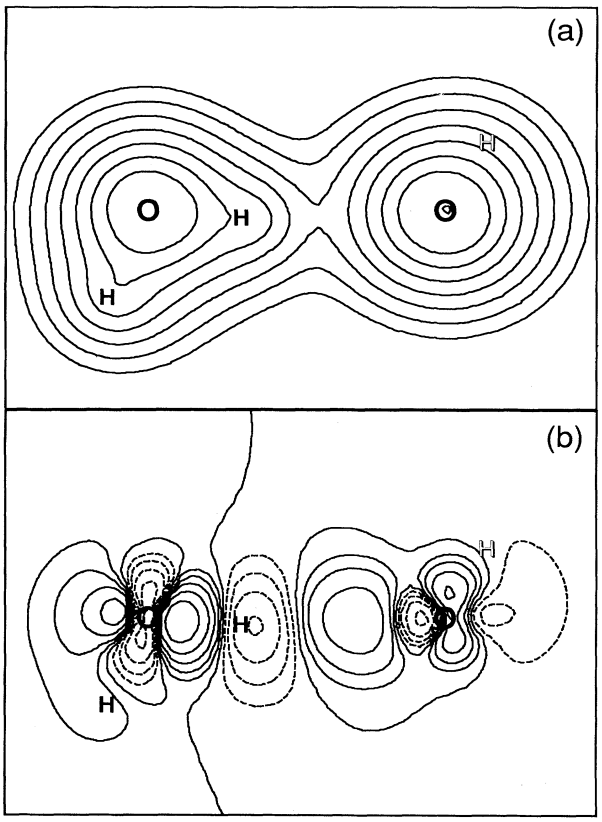

FIG. 2. Isodensity contour plots of the total density (a) and the density difference (b), $\Delta\rho=\rho[(H_2O)_2]-2\rho(H_2O)$, for the $(H_2O)_2$ molecule in the equilibrium configuration. Results are shown in the plane containing the nuclei of the proton donor (left-hand side) and the oxygen atom of the proton acceptor (right-hand side). The densities were calculated using LDA with $E_{pwc}=96$ Ry. The numerical values of the contours of $\rho=10^{-2}\times 2^n$ (a.u.), $n=0,1,\ldots,7$ and of $\Delta\rho=0\pm 10^{-3}\times 2^n$ (a.u.), $n=0,1,\ldots,5$. Solid and dashed lines in (b) correspond to $\Delta\rho\geq 0$ and $\Delta\rho<0$, respectively.

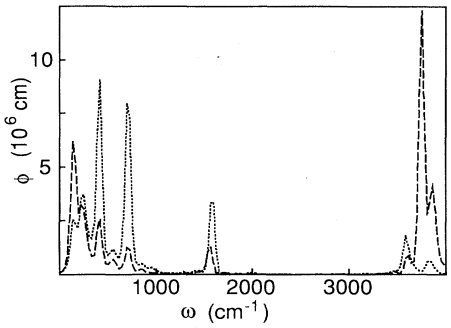

FIG. 3. Fourier transforms of the velocity correlations functions ϕ of the donor (dotted) and acceptor (dashed) molecules in $(H_2O)_2$, obtained from a 12-ps BO-LDA-MD dynamical simulation; Gaussian smoothing with $\sigma=25$ cm^{-1} was used. Frequencies larger than 3500 cm^{-1} correspond to intramolecular OH stretch modes, those $\sim$1560 cm^{-1} correspond to intramolecular bending. Frequencies below $\sim$800 cm^{-1} correspond to intermolecular vibrational modes of the dimer molecule (denoted ν_7–ν_{12} in Table II).

than negative, frequency shift of the two intramolecular stretch modes, while the shifts of the bending modes are given correctly.

The frequencies of the intermolecular modes (labeled ν_7–ν_{12} in order of decreasing frequency) are in good agreement with those obtained by Sim *et al.*[49] (where the characters of the modes are described), and are in reasonable agreement with experiment. Our predicted low-frequency modes (ν_7–ν_9) are lower than those of Sim *et al.* and are closer to experiment, perhaps due to anharmonic effects. Much of the remaining difference between our results and experiment might be removed by a self-consistent inclusion of the exchange-correlation-gradient correction to LSD, which, as found in Ref. 49, tends to shift the frequencies to smaller values.

C. Dimer transition structures and dynamics

While microwave spectroscopy[51,53] has established a C_s equilibrium geometry for the water dimer (see Fig. 1), as discussed by Dyke[52] using permutation-inversion group theory, there are eight equivalent structures which, excluding exchange of hydrogen atoms between monomers, involve interchange of hydrogen atoms within the $(H_2O)_2$ molecule, including rearrangements that interchange donor and acceptor molecules [see Refs. 48, 52, and 58, and our discussion of the dynamics of $(H_2O)_2$ given below]. Understanding of experimental results pertaining to rotational and vibrational spectra of $(H_2O)_2$ requires knowledge of the energetics and mechanisms of such interchanges, that is, knowledge of the dynamics of the transformations between the equivalent structures, and energetic and structural characterization of the transition states connecting them.

Most recently, Smith *et al.*,[48] using *ab initio* quantum-mechanical calculations, have characterized the transition structures of the water dimer connecting the eight equivalent forms. In order to further evaluate the reliability of our method, we have chosen a subset of these transition structures and compare our results with those of Smith *et al.* below and in Table III.

The transition structures we have chosen for comparison with the results of Smith *et al.* are structures 3*, 4*, 6*, and 9* (in the notation of Ref. 48). We denote the transition structure by an asterisk. In this notation, structure 1 (denoted as 1a in Ref. 48, to distinguish it from the other seven equivalent forms of the dimer) is a global minimum-energy structure (see Fig. 1), and, as discussed, in Ref. 48, transition structures 4* and 9* are first-order saddle points of the potential-energy surface, while transition structure 3* is a second-order saddle point, which is close structurally and energetically to a first-order saddle-point transition structure 2*. Each of these transition structures can be obtained by minimizing the energy with constrained symmetry (see Fig. 4). Our

TABLE III. Calculated dipole moment μ (in units of Debye) and energy differences E_s-E_1 (in kcal/mol), where $s=1$ is the equilibrium ground state of the dimer and $s=3^*$, 4^*, 6^*, and 9^* are transition structures (see Fig. 4). Results in the row marked 2(H_2O) correspond to ΔE_b, the binding energy of the dimer (see also Table II), and results corresponding to the high-dipole configuration of the dimer are given in the row marked 1(hd). For our calculations, results obtained for two values of the plane-wave cutoff energy (62 and 96 Ry) are given, and for the larger one exchange-correlation gradient corrections to the LSD results (marked LSD+xcg) are also shown.

		$E_{pwc}=62$ Ry	$E_{pwc}=96$ Ry		Smith *et al.*[a]	
Structure	μ	LSD	LSD	LSD+xcg	$MP2/6-311+G(d,p)$	+BSSE
1	2.57	0	0	0	0	0
3*	3.24	0.96	1.06	0.82	0.68[b]	0.80[c]
4*	0	1.05	1.18	1.57	1.24	1.58
6*	0	1.99	1.98	2.50	1.53[b]	
9*	3.88	3.97	3.66	2.50	1.60	1.94
2(H_2O)		9.18	9.06	4.90	6.10	
1(hd)	3.88	0.84	0.78	0.63		

[a]Reference 48.
[b]$MP2/6-31+G(d,p)$ results in Ref. 48.
[c]Using the BSSE correction of Structure 2*, in Ref. 48.

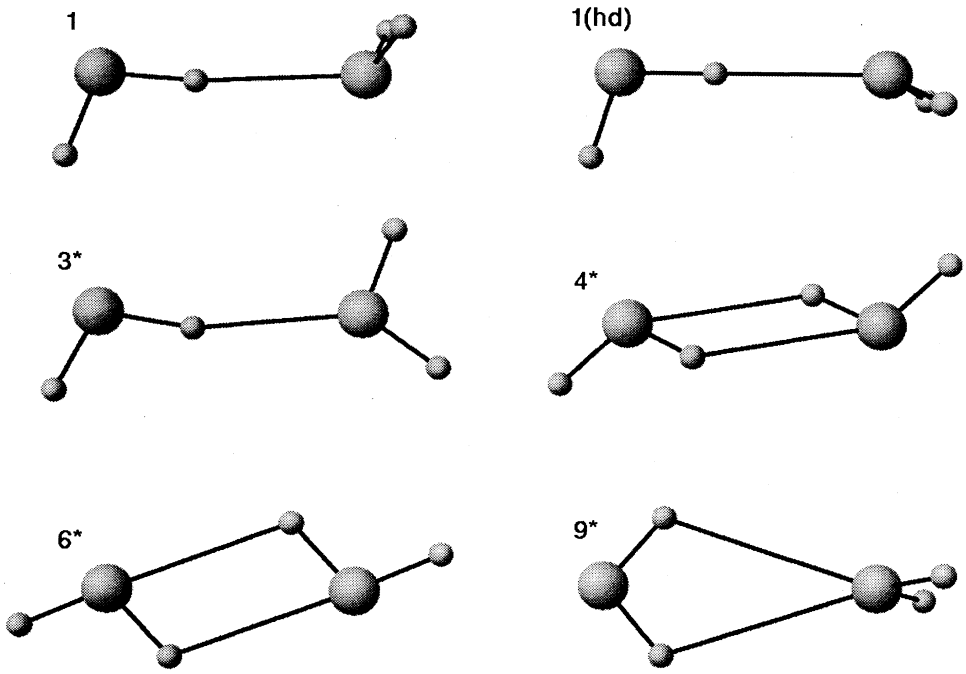

FIG. 4. Structures of the equilibrium configuration 1, high-dipole isomer 1(hd), and transition structures 3*, 4*, 6*, and 9* (in the notation of Ref. 48). 3* is planar with C_s symmetry, 4* is cyclic with C_i symmetry, 6* is planar cyclic with C_{2h} symmetry, and 9* is bifurcated with a C_{2v} symmetry.

results for these structures are given in Table III, along with the $MP2/6-311+G(dp)$ optimized results of Smith *et al.* The results are in reasonable good agreement, particularly considering the sensitivity of the results given in Ref. 48 to the level of theory used in the calculations. Additionally we note that in most cases the agreement is improved by the post-LSD exchange-correlation gradient corrections. The geometries of the transition structures are very close to those of Ref. 48 except that before applying an exchange-correlation gradient correction, the hydrogen-bonded O_DH distances are 5–10 % smaller than those given in Ref. 48 (see Table IV).

In the course of our investigation of the water-dimer potential-energy surface we have identified another potentially important isomer which we label structure 1(hd). This structure (see Fig. 4) has the C_s symmetry of the minimum-energy structure, but with the acceptor angle $\theta_A = 210°$ (instead of $\theta_A \simeq 120°$ in the equilibrium structure). The potential-energy surface about this structure is extremely flat and it is only 0.78 kcal/mol above the global minimum (0.63 kcal/mol with post-LSD exchange-correlation gradient corrections), while the dipole moment of $\mu = 3.88D$ of the 1(hd) isomer is ~50% larger than that of the equilibrium structure. The variation of energy and dipole moment with acceptor angle θ_A are shown in Fig. 5. It is of interest to remark that we have previously noted,[19(b),59] using an empirical electron-water pseudopotential, that a water dimer in this high-dipole configuration could attach an excess electron to form $(H_2O)_2^-$, with a vertical binding energy of 0.3 kcal/mol, while the experimental estimates from photoelectron spectroscopy[60] range from 0.4 to 0.7 kcal/mol. However, in this earlier study (where the $RWK2/M$ semiempirical potential[61] was employed) the energy of the 1(hd) isomer was 0.94 kcal/mol above that of the equilibrium structure

TABLE IV. Calculated geometrical parameters (distances in Å and angles in degrees) of $(H_2O)_2$ transition structures 3*, 4*, 6* and 9* (see also Table III and Fig. 4), and of the high-dipole form of the dimer 1(hd). Results for the equilibrium structure (1) are also included. The results given in the table were obtained using $E_{pwc} = 96$ Ry. For definitions of the geometrical parameters, see Fig. 1.

	Structure					
	1	1(hd)	3*	4*	6*	9*
ϕ_D	106.10	107.09	107.28	107.42	107.45	101.59
$r(O_DH_1)$	0.980	0.975	0.976	0.967	0.968	0.963
$r(O_DH_2)$	0.961	0.960	0.958	0.959	0.958	0.963
ϕ_A	106.17	106.77	107.88	107.42	107.45	105.74
$r(O_AH_1)$	0.961	0.961	0.962	0.967	0.968	0.961
$r(O_AH_2)$	0.961	0.961	0.959	0.959	0.958	0.961
$r(O_DO_A)$	2.70	2.73	2.68	2.59	2.51	2.80
θ_D	4.84	0.11	9.98	44.48	48.06	50.79
θ_A	120.56	210.0	162.72	90.07	101.41	180.0

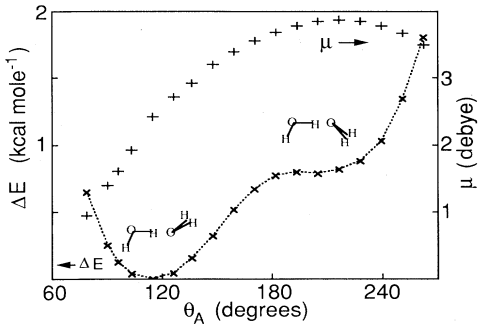

FIG. 5. Variations of the energy ΔE in kcal/mol [relative to the energy of the equilibrium structure of $(H_2O)_2$] and dipole moment μ (in units of Debye) of the $(H_2O)_2$ molecule vs acceptor angle θ_A (see Fig. 1). The structures of the equilibrium configuration (at θ_A 120.6°) and high-dipole 1(hd) configuration (at $\theta_A = 210°$, see also Fig. 4) are indicated.

(1) and thus the negatively charged cluster in the high-dipole configuration was predicted to be unstable (or metastable). Since the present calculation predicts a higher dipole moment for the 1(hd) isomer and a lower barrier for the transition from the equilibrium structure (1) into the high-dipole 1(hd) configuration, it is plausible that the high-dipole configuration of the negatively charged dimer is indeed stable and may explain the experimentally measured vertical binding energy, as we concluded before.[19(b),59]

To investigate the dynamics of transformations between equivalent structures of the $(H_2O)_2$ molecule we performed BO-LDA-MD simulations (that is, classical dynamics of the nuclei on the ground-state Born-Oppenheimer surface, as described in Sec. II). In Figs. 6 and 7 we show results of a simulation where, starting from the equilibrium geometry (structure 1a, see Fig. 1), random velocities where assigned to the nuclei and the

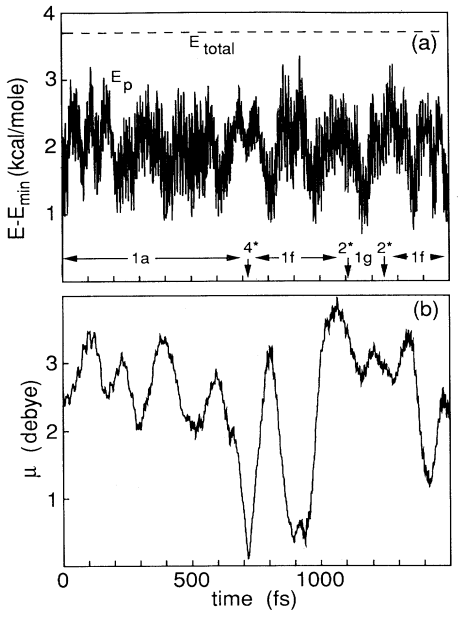

FIG. 6. Time records of energies [in (a) units of kcal/mol] and dipole moment μ [in (b) units of Debye], obtained from a dynamical BO-LDA-MD simulation of $(H_2O)_2$. The total energy E_{total} is conserved to better than 10^{-4}% of the total energy. The envelope of fluctuations in the potential energy E_p and of the dipole moment correspond to structural fluctuations and transformations. A sequence of transitions, 1a→4* →1f→2*→1g→2*→1f, is denoted at the bottom of (a); see corresponding structures in Fig. 7.

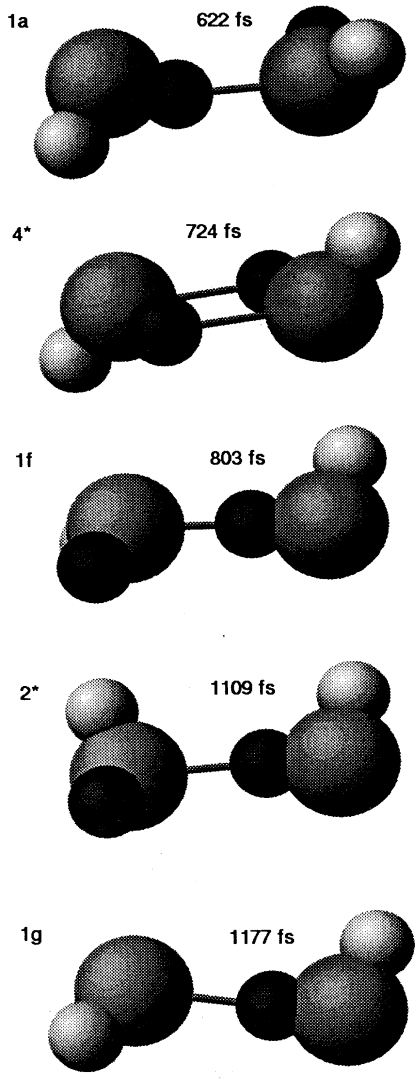

FIG. 7. Sequence of structures of $(H_2O)_2$ observed during the dynamical simulation described in Fig. 6. Structures of the sequence 1a→4*→1f→2*→1g are shown. Structure 1a corresponds to the equilibrium structure recorded at $t = 622$ fs (see Fig. 6). Transition structure 4* was recorded at $t = 724$ fs. Structure 1f, representing an exchange of the acceptor and dimer relative to the initial 1a structure, was recorded at $t = 803$ fs. Transition structure 2* (of which 3* is a planar version, see Fig. 4) was recorded at $t = 1109$ fs, and structure 1g, where the hydrogen atoms of the acceptor molecule in 1f are interchanged, was recorded at $t = 1177$ fs.

linear and angular momenta were zeroed such that the vibrational-energy content of the molecule was ~ 4.56 kcal/mol [i.e., if equipartitioned, the average energy per dynamical degree of freedom (12 in number) would be ~ 0.38 kcal/mol, which is below the barrier heights for any of the transition structures we calculated; see Table III]. The calculated average kinetic energy of the nuclei during the 1.5-ps simulation, corresponds to an estimated kinetic temperature of ~ 146 K.

As seen in Figs. 6 and 7, due to thermal fluctuations and anharmonic couplings, the system dynamically explores various regions of the potential-energy surface during the simulation, and transitions between equivalent structures of the dimer occur. The sequence of transformations shown in Figs. 6 and 7 is 1a$\rightarrow$4* $\rightarrow$1f$\rightarrow$2*$\rightarrow$1g$\rightarrow$2*$\rightarrow$1f, where an asterisk denotes a transition structure and the equivalent structures of $(H_2O)_2$ are denoted after Ref. 48 [1a is the starting equilibrium structure (see Fig. 1); 1f is like structure 1a but with the donor and acceptor molecules permuted; and structure 1g is like 1f but with the hydrogen atoms of the acceptor molecule exchanged]. We observe that these transformations involved transition structures 2* and 4* (as mentioned before, transition structure 3* is a planar version of 2*, and the barriers associated with these transition structures are close to each other).

In other simulations, where the vibrational-energy content of the $(H_2O)_2$ molecule was higher (8.44 kcal/mol), we observed transitions that resulted in scrambling of the equivalent structures of the molecule, involving mostly transition structures 2* and 4*, although occasionally transformations involving transition structures 7* and 9*, which are characterized by higher barriers (see Table III and Fig. 4 for 9*, transition structure 7* not shown) were observed. In this context we also note that during these dynamical simulations we have also observed transitions from 1a$\rightarrow$1(hd).

IV. SUMMARY

In this paper, a method for molecular-dynamics simulations on the ground-state Born-Oppenheimer electronic potential-energy surface was described. In this method the dynamics of the nuclei are obtained via integration of the classical (Newtonian) equations of motion with the total electronic energy and forces on the ions calculated for each nuclear configuration via iterative solution of the Kohn-Sham equations, within the LDA (LSDF, if required). The interactions between the electrons and the ions are described by nonlocal norm-conserving pseudopotentials, and a plane-wave basis set is used. Evaluations of the various terms in the Hamiltonian, and the operations on the wave functions, are performed using a dual-space formalism, with the Kleinman-Bylander decomposition performed in real space.

Since the electronic energy and forces on the nuclei are calculated during a dynamical simulation for each nuclear configuration, we are assured to remain on the ground-state BO surface throughout, thus allowing a relatively large integration time step τ of the nuclear equations of motion (determined by the highest characteristic vibrational frequencies in the system; thus, while in our simulations of water systems we used $\tau=0.4$ fs, simulations of alkali-metal clusters were formed with $\tau\approx 5-10$ fs, using the Gear fifth-order predictor-corrector algorithm, and conserving energy to $\sim 10^{-4}\%$ of the total energy).

The method as described in detail in Sec. II is designed for investigations of finite systems (clusters), although the generalization to infinite, periodic, systems is straightforward. When applied to investigations of a finite system the method does not employ a supercell (that is, the system is not replicated), thus allowing efficient studies of systems that may possess or develop large multipole moments, while avoiding the need for the large length scale that would be necessary in a supercell method in order for the interactions between images to vanish. The method was demonstrated via a comprehensive study of the water-molecular dimer $(H_2O)_2$ which is a prototype system for investigations of hydrogen bonding. Moreover, this system presents a computational challenge, since it involves both strong chemical bonds (intramolecular, H_2O) as well as weak hydrogen bonding between the proton donor and the acceptor molecules, and has been the subject of numerous theoretical and experimental studies. Additionally, LDA [or LSDF, as in our previous study of $Na(H_2O)_n$, $1\leq n\leq 6$] calculations of this system, using pseudopotentials and a plane-wave basis, are a particularly severe test of the applicability and accuracy of the method.

Our study shows that most satisfactory results are obtained by our calculations (when compared to experimental data and those obtained by high-level *ab initio* quantum-chemical calculations). We also note that to achieve an accurate prediction for the hydrogen-bond energy [i.e., dissociation energy of $(H_2O)_2$ into two separated monomers], and for the distance between the oxygens of the hydrogen-bonded molecules in the dimer, it is necessary to evaluate exchange-correlation gradient (xcg) corrections, which we performed in a post-LDA mode.

In addition to the equilibrium energetics, structure and dynamics of $(H_2O)_2$, we have studied transition structures connecting equivalent structures of the dimer molecule, and our results for the properties of these states and potential-energy barriers between them and the equilibrium configuration, compare well with previous calculations. Additionally, in the course of these calculations we have identified a high-dipole isomer of the $(H_2O)_2$ molecule (see Fig. 4), which may play a role in formation of the negative molecular ion $(H_2O)_2^-$.

To investigate the dynamics of transitions between the equivalent structures, and demonstrate our method, we performed molecular-dynamical simulations on the electronic ground-state BO surface (BO-LDA-MD). These simulations illustrate the dynamical mechanisms of interchanges between equivalent structures, involving certain of the proposed transition structures.

ACKNOWLEDGMENT

Research supported by the U.S. Department of Energy Grant No. FG05-86ER-45234. Calculations were per-

formed on Cray-YMP computers at the Florida State University Computing Center, at the National Energy Research Supercomputer Center, Livermore, California, and the Pittsburgh Supercomputing Center.

APPENDIX A: DENSITY MIXING TO ACHIEVE SELF-CONSISTENCY

In the solution of the KS-LSD equations, self-consistency can be achieved by using an iterative density-mixing scheme. In this procedure, the Hamiltonian for the ith iteration is obtained from the results of previous iterations of the KS equation as follows:

$$\hat{H}_\sigma^{(i)}\psi_{j\sigma}^{(i)}=\epsilon_{j\sigma}^{(i)}\psi_{j\sigma}^{(i)}, \quad i\geq 0 , \tag{A1}$$

$$\Delta\rho_\sigma^{(i)}(\mathbf{r})=\sum_j f_{j\sigma}^{(i)}|\psi_{j\sigma}^{(i)}|^2-\rho_\sigma^{(i)}(\mathbf{r}) , \tag{A2}$$

where $\hat{H}_\sigma^{(i)}=\hat{H}_\sigma(\{\mathbf{R}_I\},\rho_+^{(i)},\rho_-^{(i)})$, the occupation factors $f_{j\sigma}^{(i)}$ are obtained using a Fermi function with the eigenvalues $\epsilon_{j\sigma}^{(i)}$, and $\rho_\sigma^{(i)}(\mathbf{r})$ is the "input" density from the previous iteration; the density in the $(i+1)$th iteration is constructed as

$$\rho_\sigma^{(i+1)}(\mathbf{r})=\rho_\sigma^{(i)}(\mathbf{r})+\sum_{\sigma'}\int d^3r' G^{(i)}(\mathbf{r},\sigma;\mathbf{r}',\sigma')\Delta\rho_{\sigma'}^{(i)}(\mathbf{r}') . \tag{A3}$$

In simple mixing, $G^{(i)}(\mathbf{r},\sigma;\mathbf{r}',\sigma')=\alpha_\sigma\delta(\mathbf{r}-\mathbf{r}')\delta_{\sigma,\sigma'}$, where $0<\alpha_\sigma<1$ is a mixing parameter. We use the modified Broyden's method,[62] in which $G^{(i)}$ is an approximation to the inverse Jacobian obtained from $\{\rho_\sigma^{(j)},\Delta\rho_\sigma^{(j)}\}$ for all previous iterations $j<i$.

Self-consistency is achieved when $\Delta\rho_\sigma^{(i)}(\mathbf{r})=0$, or in practice when

$$\sum_\sigma\int d^3r|\Delta\rho_\sigma^{(i)}|^2\leq C , \tag{A4}$$

where C is the convergence criteria. Fewer iterations are required to achieve a self-consistent solution when the initial guess, $\rho_\sigma^{(0)}$, is as close as possible to the final converged value. We have found that in a molecular-dynamics simulation (i.e., when dynamical evolution of the ions on the Born-Oppenheimer potential-energy surface is calculated) a good estimate for the initial electronic density at time $t+\tau$ (where τ is the time step used in integrating the ionic equations of motion) can be obtained from a Taylor series in time, using the converged densities corresponding to previous time steps to estimate the time derivatives.

An alternative method that can be used in structure optimization as well as in molecular-dynamics simulations, is to estimate the density by

$$\rho(\mathbf{r};\{\mathbf{r}_I(t)\})=\sum_{j=1}^{n_t} a_j\rho[\mathbf{r};\{\mathbf{r}_I(t_j)\}] , \tag{A5}$$

where $t_j<t$ indicates previous steps in a structure optimization process, or $t_j=t-j\tau$, where τ is the time step used in integration of the equations of motion of the nuclei. The coefficients a_j are obtained by minimization (e.g., via a least-square-fit algorithm) of the quantity

$$F(\{a_j\})=\sum_I\left|\mathbf{r}_I(t)-\sum_{j=1}^{n_t}a_j\mathbf{r}_I(t_j)\right|^2 . \tag{A6}$$

Finally, we find that in some situations the density-mixing iterative process will not converge to the desired degree. In these situations we find it helpful to add some random noise to the trial density and to the wave functions (see Appendix B) and restart the process.

APPENDIX B: SOLVING FOR EIGENFUNCTIONS OF THE KOHN-SHAM EQUATION

The most difficult and time consuming part of the calculation of the electronic energy is finding the eigenfunctions and eigenvalues of the KS Hamiltonian for a given trial density. This must be done accurately to achieve convergence of the self-consistency iterative density-mixing scheme (Appendix A) and to ensure sufficient accuracy of the calculated total energy and forces on the ions.

We need to solve for the lowest n_s eigenfunctions of the KS-LSD equations, where n_s is larger or equal to the number of valence electrons of spin σ (n_s is typically in the range $10-10^3$, while we may have 10^4-10^6 plane waves in the basis set). To this end we have developed a Block-Davidson-type method,[14,15] which we outline below.

We begin with n_s initial estimates of the lowest eigenfunctions, $\psi_j^{(0)}$, $j=1,\ldots,n_s$ (usually these wave functions are taken from a previous MD or minimization step, or a KS iteration), and n_x "extra" wave functions, $\psi_j^{(0)}$, $j=n_s+1,\ldots,n_s+n_x$ (these, typically, are linear combinations of the solutions of previous MD or minimization steps and/or KS iterations and, if appropriate, the solutions for the other spin manifold). The $\psi_j^{(0)}$'s are normalized but not necessarily orthogonal.

(a) Calculate the $n_b\times n_b$ subspace Hamiltonian and overlap matrices, for $n_b=n_s+n_x$:

$$H_{ij}=\langle\psi_i^{(0)}|\psi_j'^{(0)}\rangle=H_{ji} , \tag{B1}$$

$$S_{ij}=\langle\psi_i^{(0)}|\psi_j^{(0)}\rangle=S_{ji} , \tag{B2}$$

where $\psi_j'=\hat{H}_j$ [see Eqs. (41)–(43)].

(b) Solve the generalized eigenvalue problem (using available library routines)

$$(\underline{\underline{H}}-\epsilon_j^{(0)}\underline{\underline{S}})\underline{\chi}_j^{(0)}=0 , \tag{B3}$$

where the transpose of the vector $\underline{\chi}_j^{(0)}$ is given by

$$\underline{\chi}_j^T=(\chi_{1j},\chi_{2j},\ldots,\chi_{n_bj}) . \tag{B4}$$

(c) Define the input wave functions for iteration number 1.

$$\psi_j^{(1)}=\sum_{i=1}^{n_b}\chi_{ij}^{(0)}\psi_i^{(0)} \quad \text{for } j=1,\ldots,n_s . \tag{B5}$$

The Jth iteration begins with n_p orthonormal wave functions $\psi_j^{(J)}$, $j=1,\ldots,n_p$ ($n_p\geq n_s$, $n_p=n_s$ for $J=1$), and

$$H_{ij}=\epsilon_j^{(J-1)}\delta_{ij} \quad \text{and} \quad S_{ij}=\delta_{ij} \quad \text{for } j=1,\ldots,n_p \ . \tag{B6}$$

(a) Compute the "residual wave functions,"

$$R(\psi_j^{(J)},\epsilon_j^{(J-1)})=(\hat{H}-\epsilon_j^{(J-1)})\psi_j^{(J)} \tag{B7}$$

for $j=1,\ldots,n_s$ ($\epsilon_j \le \epsilon_{j+1}$).

(b) Perform a convergence test, that is, evaluate

$$|R(\psi_j^{(J)},\epsilon_j^{(J-1)})| < R_{\max} \tag{B8}$$

for $j=1,\ldots,n_s$, with typically $R_{\max}=10^{-5}$. When the inequality in Eq. (B8) is satisfied, the iterative solution of the Hamiltonian has converged. If the convergence test Eq. (B8) fails, then

(c) add n_s additional normalized wave functions to the subspace, defined by

$$\psi_{n_p+j}^{(J)}=(\hat{D}_j^{(J-1)})^{-1}R(\psi_j^{(J)},\ \epsilon_j^{(J-1)})/|\psi_{n_p+j}^{(J)}| \ , \qquad j=1,\ldots,n_s \ , \tag{B9}$$

where $\langle \mathbf{g}|\hat{D}_j^{(J-1)}|\mathbf{g}'\rangle=\delta_{\mathbf{g},\mathbf{g}'}[\langle \mathbf{g}|\hat{H}|\mathbf{g}\rangle-\epsilon_j^{(J-1)}]$. In some situations (i.e., if the residuals $|R(\psi_j^{(J)},\epsilon_j^{(J-1)})|$ are not decreasing or are decreasing very slowly with increasing iteration number J) it is helpful to also add $n_x \ge 0$ additional random (normalized) wave functions to the subspace.

(d) Set $n_b=n_p+n_s+n_x$, and calculate the unknown elements of the subspace Hamiltonian and overlap matrices: H_{ij}, Eq. (B1) and S_{ij}, Eq. (B2) for $i=1,\ldots,n_b$ and $j=n_p+1,\ldots,n_b$.

(e) Solve the generalized eigenvalue problem, Eqs. (B3) and (B4).

(f) Determine n_p for the next iteration: $n_p=n_b$; or, if $n_b \ge n_{\max}$, then $n_p=n_s$ (i.e., start over as if from the first iteration, $J=1$).

(g) Calculate the input wave functions for the next iteration $\psi_j^{(J+1)}$, $j=1,\ldots,n_p$ [see Eq. (B5)].

$$\psi_j^{(J+1)}=\sum_{i=1}^{n_b}\chi_{ij}^{(J)}\psi_i^{(J)}, \quad j=1,\ldots,n_p \ . \tag{B10}$$

APPENDIX C

In this appendix we will discuss two methods of obtaining the wave function on the real-space grid [the S grid, see Eqs. (28) and (32)].

The first method is implied by the following equation (assuming $M_\alpha=2N_\alpha$):

$$\phi_{j\sigma}(\mathbf{s}+\mathbf{t})=(8N)^{-1/2}\sum_{\mathbf{g}} e^{i\mathbf{g}\cdot\mathbf{t}}\tilde{\phi}_{j\sigma}(\mathbf{g})e^{i\mathbf{g}\cdot\mathbf{s}} \ , \tag{C1}$$

where

$$\mathbf{s}=(n_xL_x/N_x,n_yL_y/N_y,n_zL_z/N_z), \quad 0\le n_\alpha<N_\alpha-1 \ , \tag{C2}$$

and

$$\mathbf{t}=\tfrac{1}{2}(j_xL_x/N_x,j_yL_y/N_y,j_zL_z/N_z), \quad j_\alpha=0,1 \ . \tag{C3}$$

Note that the s grid (the dual of the g grid) has spacing $\Delta_\alpha=L_\alpha/N_\alpha$ which is twice that of the S grid. The S grid is obtained via the eight translations, $\{\mathbf{t}\}$ of Eq. (C3), of the s grid.

The second method requires a definition of the wave function on the G grid (Eqs. 26):

$$\tilde{\phi}_{j\sigma}(\mathbf{G})=\tilde{\phi}_{j\sigma}(\mathbf{G}) \quad \text{for } |\mathbf{G}|\le g_{\max} \ , \qquad =0 \quad \text{for } g_{\max}<|\mathbf{G}|\le 2g_{\max} \ . \tag{C4}$$

Using Eq. (C4) we may write for the wave function on the S grid

$$\phi_{j\sigma}(\mathbf{S})=M^{-1/2}\sum_{\mathbf{G}}\tilde{\phi}_{j\sigma}(\mathbf{G})e^{i\mathbf{G}\cdot\mathbf{S}} \ . \tag{C5}$$

In order to assess the merits of the two methods, let us suppose that $N_\alpha=2^{P_\alpha}$ for all α (x, y, and z). Then a one-dimensional (1D) FFT in the αth direction, such as required in the first method, takes $\mathcal{O}(N_\alpha P_\alpha)$ operations, while the 1D FFT's required in the second method take $\mathcal{O}[2N_\alpha(P_\alpha+1)]$ operations.

In the first method, if one uses a 3D FFT routine eight times (for the eight translations $\mathbf{t}$), the number of operations required is $\mathcal{O}[8N_xN_yN_z(P_x+P_y+P_z)]$ plus $\mathcal{O}(8N_xN_yN_z)$ to obtain the set $\{e^{i\mathbf{t}\cdot\mathbf{g}}\tilde{\phi}_{j\sigma}(\mathbf{s})\}$ for a particular $\mathbf{t}$. In comparison, using a 1D FFT routine and, e.g., performing first the FFT operation in the x direction for the two values of t_x, then the y direction FFT's for the four values of (t_x,t_y), etc., the number of operations is reduced to $\mathcal{O}[N_xN_yN_z(2P_x+4P_y+8P_z)]$ for the FFT's and $\mathcal{O}(7N_xN_yN_z)$ for the translations.

In the second method, a 3D FFT would take $\mathcal{O}[8N_xN_yN_z(P_x+P_y+P_z+3)]$ operations while by using 1D FFT's the requirement can be reduced to $\mathcal{O}[N_xN_yN_z(2P_x+4P_y+8P_z+14)]$.

Thus, it appears that the first method may be slightly more efficient. However, the advantage, if any, is small, and there is more "bookkeeping." The advantages of the second method are a simpler code, particularly in being able to handle both even and odd values of N_α. In addition, using this method, it is easier to avoid memory-bank conflicts due to an even stride (an important consideration on many computers, e.g., Cray 2 and Cray YMP).

APPENDIX D

The Hartree energy term, Eq. (15), is evaluated on the real-space S grid, Eqs. (28), in the spirit of the ansatz Eq. (37), using the expression

$$\epsilon_H(\mathbf{S})=\frac{1}{2}\sum_{\mathbf{S}'}[D_+(\mathbf{S}')+D_-(\mathbf{S}')]U_c(\mathbf{S}-\mathbf{S}') \ , \tag{D1a}$$

where

$$U_c(\mathbf{S})=|\mathbf{S}|^{-1} \quad \text{for } |\mathbf{S}|\neq 0 \ , \tag{D1b}$$

and

$$U_c(\mathbf{0})=\int_{-\Delta x/2}^{\Delta x/2}dx\int_{-\Delta y/2}^{\Delta y/2}dy\int_{-\Delta z/2}^{\Delta z/2}dz\,(x^2+y^2+z^2)^{-1/2} \ . \tag{D1c}$$

This calculation amounts to replacing the density $\rho_\sigma(\mathbf{r})$ with a set of charges $\{-D_\sigma(\mathbf{S})\}$ located at the grid points. The singularity is treated by spreading the charge uniformly over the volume associated with the grid point. To assess the accuracy of our results, we have experimented by adding gradient corrections to $\epsilon_H(\mathbf{S})$. However, for a value of $g_{\max}$ large enough to achieve convergence, we found that such gradient corrections to $\epsilon_H(\mathbf{S})$ made a negligible difference.

Using Eqs. (D1), the values of $\epsilon_H(\mathbf{S})$ on the S-grid points are evaluated efficiently via a convolution in reciprocal space. We define

$$U_c^P(\mathbf{S}+\mathbf{T})=U_c(\mathbf{S}) , \tag{D2}$$

where $\mathbf{T}=2(p_xL_x,p_yL_y,p_zL_z)$, $p_\alpha=0,\pm1,\ldots$, so that U_c^P is periodic, with periods $2L_\alpha$. The discrete Fourier transform of U_c^P is

$$\overline{U}_c^P(\mathbf{Q})=\sum_{\mathbf{S},\mathbf{T}} U_c^P(\mathbf{S}+\mathbf{T})e^{-i\mathbf{Q}\cdot(\mathbf{S}+\mathbf{T})} , \tag{D3}$$

where the sum over $\mathbf{T}$ includes only $p_\alpha=0,1$. The reciprocal-space grid for $\mathbf{Q}$ is given by

$$\mathbf{Q}=\pi(q_x/L_x,q_y/L_y,q_z/L_z) , \tag{D4}$$

where $q_\alpha=0,1,\ldots,2M_\alpha-1$ [see also Eqs. (26)]. We also define

$$\overline{D}_\sigma(\mathbf{Q})=(8M)^{-1/2}\sum_{\mathbf{S}} D_\sigma(\mathbf{S})e^{-i\mathbf{Q}\cdot\mathbf{S}} . \tag{D5}$$

With these definitions, the Hartree energy term, $\epsilon_H(\mathbf{S})$ on the S grid, is given by

$$\epsilon_H(\mathbf{S})=(8M)^{-1/2}\sum_{\mathbf{Q}} [\overline{D}_+(\mathbf{Q})+\overline{D}_-(\mathbf{Q})]\overline{U}_c^P(\mathbf{Q})e^{i\mathbf{Q}\cdot\mathbf{S}} . \tag{D6}$$

[1]M. P. Allen and D. J. Tildesley, *Computer Simulations of Liquids* (Oxford University Press, Oxford, 1987).

[2]*Atomistic Simulations of Materials: Beyond Pair Potentials,* edited by V. Vitek and D. J. Srolovitz (Plenum, New York, 1989).

[3]*Computer Simulations in Materials Science,* edited by M. Meyer and V. Pontikis (Kluwer, Dordrecht, 1991).

[4]*Many-Atom Interactions in Solids,* edited by R. N. Nieminen, M. J. Puska, and M. J. Manninen (Springer, Berlin, 1990).

[5]*Simulations of Liquids and Solids,* edited by G. Ciccotti, D. Frenkel, and I. R. McDonald (North-Holland, Amsterdam, 1987).

[6]J. Tersoff, Phys. Rev. **37**, 6991 (1988); S. M. Foiles, M. I. Baskes, and M. S. Daw, Phys. Rev. B **33**, 7983 (1986); K. W. Jacobsen, in *Many-Atom Interactions in Solids* (Ref. 4), p. 34.

[7]M. Born and J. R. Oppenheimer, Ann. Phys. **84**, 457 (1927).

[8]R. Car and M. Parrinello, Phys. Rev. Lett. **55**, 2471 (1985); see review by G. Galli and M. Parrinello in Ref. 3, p. 283.

[9]R. G. Parr and W. Yang, *Density-Functional Theory of Atoms and Molecules* (Oxford University Press, New York, 1989).

[10]M. C. Payne, J. D. Joannopoulos, D. C. Allan, M. P. Teter, and D. H. Vanderbilt, Phys. Rev. Lett. **56**, 2656 (1986).

[11]I. Stich, R. Car, M. Parrinello, and S. Baroni, Phys. Rev. B **39**, 4997 (1989).

[12]M. P. Teter, M. C. Payne, and D. C. Allan, Phys. Rev. B **40**, 12 255 (1989).

[13]D. C. Allan and M. P. Teter, Phys. Rev. Lett. **59**, 1136 (1987).

[14]D. M. Wood and A. Zunger, J. Phys. A **18**, 1343 (1985).

[15]E. R. Davidson, J. Comput. Phys. **17**, 87 (1975).

[16]See, e.g., B. N. Parlett, *The Symmetric Eigenvalue Problem* (Prentice-Hall, Englewood Cliffs, NJ, 1980).

[17]W. Kohn and L. Sham, Phys. Rev. **140**, A1133 (1965).

[18]A. Selloni, P. Carenvali, R. Car, and M. Parrinello, Phys. Rev. Lett. **59**, 823 (1987); A. Selloni, E. Fois, M. Parrinello, and R. Car, Phys. Scr. **T25**, 261 (1989).

[19](a) R. N. Barnett, U. Landman, A. Nitzan, and G. Rajagopal, J. Chem. Phys. **94**, 608 (1991); (b) R. N. Barnett, U. Landman, and A. Nitzan, Phys. Rev. A **38**, 2178 (1988).

[20]M. R. Pederson, B. M. Klein, and J. Q. Broughton, Phys. Rev. B **38**, 3825 (1988); M. Sprik and M. L. Klein, J. Chem. Phys. **89**, 1592 (1989).

[21](a) J. M. Soler and A. R. Williams, Phys. Rev. B **40**, 5414 (1989); (b) **42**, 9728 (1990).

[22]R. Yu, D. Singh, and H. Krakauer, Phys. Rev. B **43**, 6411 (1981).

[23]B. Hartke and E. A. Carter, J. Chem. Phys. **97**, 6569 (1992).

[24]R. N. Barnett, C. L. Cleveland, and U. Landman, Phys. Rev. Lett. **54**, 1674 (1985); *ibid.* **55**, 2035 (1985).

[25]O. F. Sankey and D. J. Miklweski, Phys. Rev. B **40**, 3979 (1989); F. S. Kahn and J. Q. Broughton, *ibid.* **39**, 3688 (1989); C. Z. Wang, C. T. Chan, and K. M. Ho, *ibid.* **42**, 11 276 (1990).

[26]J. Harris, Phys. Rev. B **31**, 1770 (1985); J. Harris and D. Hohl, J. Phys. Condens. Matter **2**, 5161 (1989).

[27]N. Troullier and J. L. Martins, Phys. Rev. B **43**, 1993 (1991).

[28]G. N. Rajagopal, R. N. Barnett, and U. Landman, Phys. Rev. Lett. **67**, 727 (1991).

[29]R. N. Barnett, U. Landman, and G. Rajagopal, Phys. Rev. Lett. **67**, 3058 (1991).

[30](a) R. N. Barnett and U. Landman, Phys. Rev. Lett. **70**, 1775 (1993); Z. Phys. D (to be published); (b) H.-P. Kaukonen, R. N. Barnett, and U. Landman, J. Chem. Phys. **97**, 1365 (1992).

[31]H.-P. Cheng, R. N. Barnett, and U. Landman, Phys. Rev. B (to be published).

[32]U. Rothlisberger and W. Andreoni, J. Chem. Phys. **94**, 8129 (1991), and references therein; R. Car, M. Parrinello, and W. Andreoni, in *Microclusters,* edited by S. Sugano, Y. Nishina, and S. Ohnishi (Springer, Berlin, 1987).

[33]R. M. Wentzcovitch and J. L. Martins, Solid State Commun. **78**, 831 (1991).

[34]D. Gunnarson and B. I. Lundqvist, Phys. Rev. B **13**, 4274 (1976).

[35](a) A. D. Becke, Phys. Rev. A **38**, 3098 (1988); (b) A. D. Becke, J. Chem. Phys. **96**, 2155 (1992).

[36]J. P. Perdew, Phys. Rev. B **33**, 8822 (1986); **34**, 7046 (1986).

[37]J. L. Martins and M. L. Cohen, Phys. Rev. B **37**, 6134 (1988); N. Troullier and J. S. Martins, *ibid.* **43**, 8861 (1991).

[38]S. Saito and M. L. Cohen, Phys. Rev. B **38**, 1123 (1988); G. W. Fernando, G.-X. Qian, M. Weinert, and J. W. Davenport, Phys. Rev. B **40**, 7985 (1989).

[39]L. Kleinman and D. M. Bylander, Phys. Rev. Lett. **48**, 1425 (1982).

[40]S. H. Vosko, L. Wilks, and M. Nusair, Can. J. Phys. **58**, 1200 (1980); S. H. Vosko, and L. Wilks, J. Phys. C **15**, 2139 (1982).

[41]D. M. Ceperley and B. J. Alder, Phys. Rev. Lett. **45**, 566 (1980).
[42]L. Fan and T. Ziegler, J. Chem. Phys. **94**, 6057 (1991); G. Ortiz and P. Ballone, Phys. Rev. B **43**, 6376 (1991).
[43]C. Lee, D. Vanderbilt, K. Laasonen, R. Car, and M. Parrinello, Phys. Rev. Lett. **69**, 462 (1992).
[44]R. D. King-Smith, M. C. Payne, and J. S. Lin, Phys. Rev. B **44**, 13 063 (1991).
[45]R. P. Feynman, Phys. Rev. **56**, 340 (1939).
[46]*Intermolecular Forces,* edited by P. L. Huyskens, W. A. Luck, and T. Zeegers-Huyskens (Springer, Berlin, 1991).
[47]M. Van Thiel, E. Becker, and G. Pimentel, J. Chem. Phys. **27**, 486 (1957).
[48]B. J. Smith, D. J. Swanton, J. A. Pople, H. F. Schaefer III, and L. Radom, J. Chem. Phys. **92**, 1241 (1990).
[49]F. Sim, A. St.-Amant, I. Papai, and D. R. Salahub, J. Am. Chem. Soc. **114**, 4391 (1992).
[50]K. S. Kim, B. J. Mhin, O.-S. Choi, and K. Lee, J. Chem. Phys. **97**, 6649 (1992).
[51]T. R. Dyke, K. M. Mack, and J. S. Muenter, J. Chem. Phys. **66**, 498 (1977).
[52]T. R. Dyke, J. Chem. Phys. **66**, 492 (1977).
[53]J. A. Odutola and T. R. Dyke, J. Chem. Phys. **72**, 5062 (1980).
[54]See Ref. 57.
[55]J. G. C. van Duijneveldt-van de Rijdt and F. B. van Duijneveldt, J. Chem. Phys. **97**, 5019 (1992).
[56]K. Morokuma and K. Kitaura, in *Molecular Interaction,* edited by H. Ratajczak and W. J. Orville-Thomas (Wiley, Chichester, 1980), Vol. 1, p. 21.
[57]See review by L. G. Vanquickenborne in Ref. 46, p. 31.
[58]L. H. Coudert and J. T. Hougen, J. Mol. Spectrosc. **130**, 86 (1988).
[59]R. N. Barnett, U. Landman, S. Dhar, N. R. Kestner, J. Jortner, and A. Nitzan, Chem. Phys. **91**, 7797 (1989).
[60](a) H. Haberland, H. G. Schindler, and D. R. Worsnop, Ber. Bunsenges. Phys. Chem. **88**, 270 (1989); (b) K. H. Bowen and J. G. Eaton, in *The Structure of Small Molecules and Ions,* edited by R. Naaman and Z. Vager (Plenum, New York, 1988), p. 147.
[61]J. R. Reimers and R. O. Watts, Chem. Phys. **85**, 83 (1984); see also R. N. Barnett, U. Landman, C. L. Cleveland, and J. Jortner, J. Chem. Phys. **88**, 4421 (1988).
[62]D. D. Johnson, Phys. Rev. B **38**, 12 807 (1988).

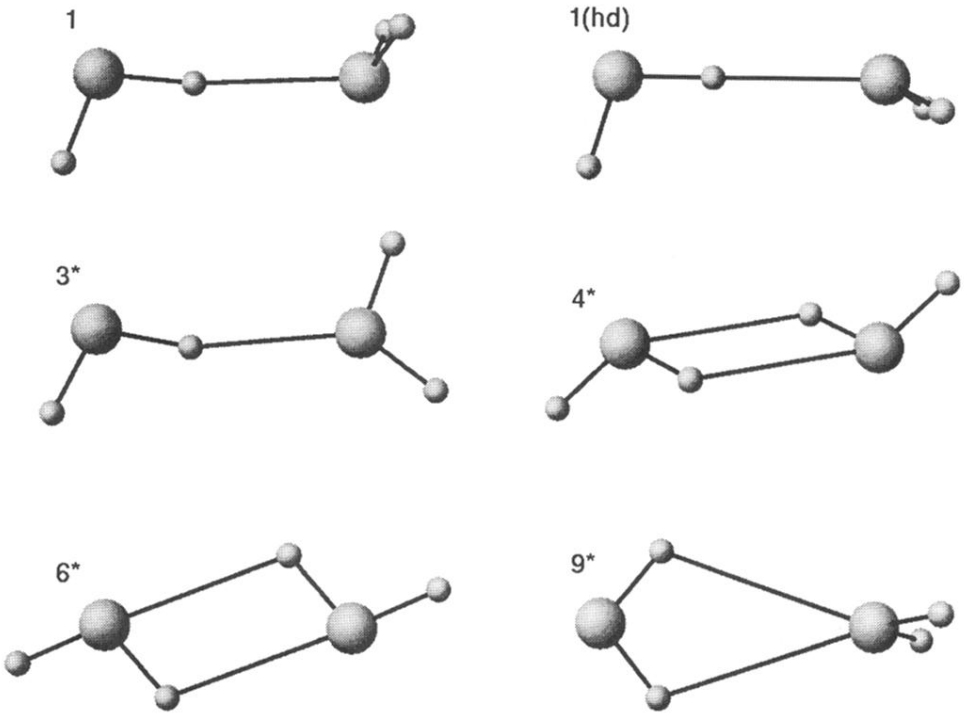

FIG. 4. Structures of the equilibrium configuration 1, high-dipole isomer 1(hd), and transition structures 3^*, 4^*, 6^*, and 9^* (in the notation of Ref. 48). 3^* is planar with C_s symmetry, 4^* is cyclic with C_i symmetry, 6^* is planar cyclic with C_{2h} symmetry, and 9^* is bifurcated with a C_{2v} symmetry.

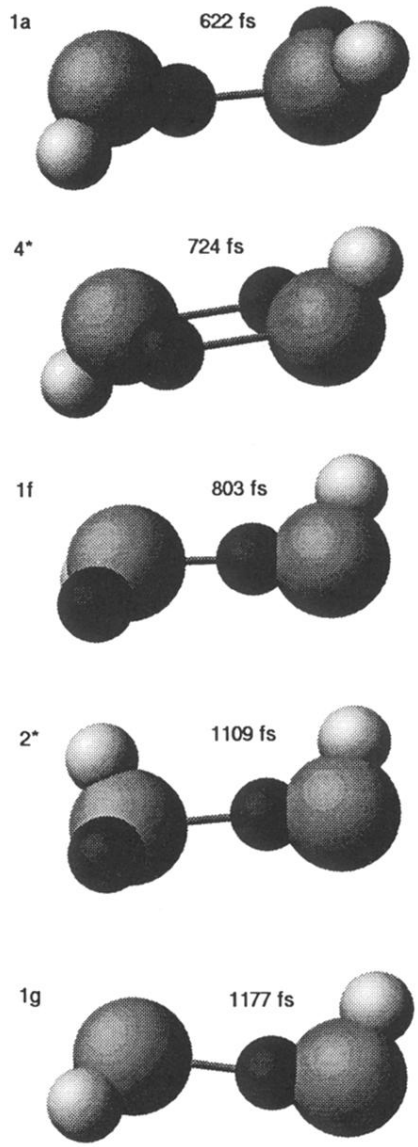

FIG. 7. Sequence of structures of $(H_2O)_2$ observed during the dynamical simulation described in Fig. 6. Structures of the sequence 1a→4*→1f→2*→1g are shown. Structure 1a corresponds to the equilibrium structure recorded at $t=622$ fs (see Fig. 6). Transition structure 4* was recorded at $t=724$ fs. Structure 1f, representing an exchange of the acceptor and dimer relative to the initial 1a structure, was recorded at $t=803$ fs. Transition structure 2* (of which 3* is a planar version, see Fig. 4) was recorded at $t=1109$ fs, and structure 1g, where the hydrogen atoms of the acceptor molecule in 1f are interchanged, was recorded at $t=1177$ fs.